1-1-2011

Shape analysis in shape space

Vahid Taimouri
Wayne State University,

Recommended Citation

Taimouri, Vahid, "Shape analysis in shape space" (2011). *Wayne State University Dissertations.* Paper 418.

SHAPE ANALYSIS IN SHAPE SPACE

by

VAHID TAIMOURI

DISSERTATION

Submitted to the Graduate School

of Wayne State University,

Detroit, Michigan

in partial fulfillment of the requirements

for the degree of

DOCTOR OF PHILOSOPHY

2012

MAJOR: COMPUTER SCIENCE

Approved by:

____

Advisor Date

____

____

____

DEDICATION

I dedicate this dissertation to my family, especially ...

to my father and mother for opening my eyes to the world
and instilling importance of hard work;

to my sisters, Sharareh, Atoosa, and Sadaf, for their
encouragement and support;

and last but not least, to my beloved nephew, Hirbod.

ACKNOWLEDGMENTS

First and foremost, I would like to thank my advisor, Dr. Jing Hua, for his continuous support and guidance in the Ph.D. program. During my Ph.D. study, he has tirelessly spent numerous hours with me discussing research, teaching me to write papers, and answering my questions. He has been available to me all the time whenever I needed his feedback. Dr. Jing Hua is an excellent role model for any young researcher to emulate. This dissertation would not have been possible without him.

I am very grateful to Dr. Farshad Fotouhi, Dr. Chandan Reddy, and Dr. Otto Muzik for serving on my dissertation committee and giving constructive suggestions and comments on the dissertation.

Also, I thank all my colleagues in Graphics & Imaging Lab, Dr. Guangyu Zou, Dr. Yunhao Tan, Dr. Chang Liu, Dr. Zhaoqiang Lai, Jiaxi Hu, and Darshan Pai, for having insightful discussions with me.

Last but not least, I deeply acknowledge the love and encouragement from my parents and my sisters. I hope I have made them all proud.

TABLE OF CONTENTS

Chapter 3 QUASI-CONFORMAL DEFORMATION CLASSIFICATION IN SHAPE SPACE . . . 26

LIST OF TABLES

LIST OF FIGURES

CHAPTER 1

INTRODUCTION

As the data acquisition methods advance rapidly, a new concern is to deal with the huge amount of data and take the desired information out of the acquired data. This necessitates the data mining techniques such as face detection, medical image analysis, deformation detection, shape classification and shape recognition. The image processing techniques always use the acquired images intensity as the classifying measure; moreover, some limiting constraints such as the rectangular frame of the image may simplify the complexity of the problem. In contrast, in the shape classification techniques various measures such as normal vector, mean curvature, Gaussian curvature, and geodesic length can be used as the classifiers. In addition, the shape topology and connectivity in the shape classification are among the issues which need to be addressed and may make the shape classification problem more intricate.

There are actually two points of view towards the shape classification. From a physical point of view, the degrees of freedom are governed by physical principles giving intuitively meaningful behavior upon the geometric substrate. For instance, the deformable models try to approximate the object deformation by minimizing the summation of the deformation energy causing the internal elastic forces, and the external potential energy function under constraint of smoothness and symmetry of the model in the Lagrangian setting ([66]). In contrast, from a geometry point of view, the shape abstraction is necessary to manage efficient matching of high dimensional shapes. Indeed the classifier must extract meaningful information from the shapes while making the weakest possible assumption about observed shapes ([94]).

The traditional perspective towards the shape abstraction is mainly based on the machine vision techniques in which a property is extracted from the surface; this feature extractor called shape descriptor may extract either global features like boundary or volume of the shape, convex-hull packing and hull compactness; or the local features like Gaussian curvature, mean curvature and edge length, which are invariant under similarity transformations. Then a metric which better represents the desired property is constructed based on bending energy or difference in curvature. At the end by minimizing the energy functional the shape is classified ([24]). However, another approach is to remove the similarity transformations from the shapes beforehand, and work with the full geometry of the shapes. Therefore, the results are more interpretable with the more geometrical information [10]. Towards this end, the modern geometry uses another concept named shape space, where coordinates of points in this space represent generalized properties associated with various geometrical properties. In the other word, each group of shapes corresponds to the same point in shape space.

Basically, the boundary of an object, a closed contour in 2D or a compact surface in 3D, defines the shape of an object. Then, k landmarks are picked from the shape to constitute a configuration of k points. Most of the geometrical information of the shape is preserved, if enough landmarks are picked from the continuous shape [61] [51]. One of the pioneer methods in landmark based shape analysis was proposed by Kendall [55] [56] showing that a specific metric, Procrustes distance, leads to a Riemannian manifold for planar triangles. Thus, the set of all planar triangles is the quotient manifold under the group of rotations, which is isometric to the surface of a 2D sphere of radius 0.5.

Depending on the application, the appropriate shape space should be constructed. For instance, left and right hands are reflected to each other, thus the reflection shape space better represents their similarity. Further, a projective shape space reveals the similarity between different photographs of the same object taken from different angles.

To carry out shape analysis on the shape space of interest, some appropriate estimation and inference tools are developed on general non-Euclidean manifolds. For instance, mean and variation defined for a general probability distribution on the manifold are employed to perform nonparametric inference on manifolds [9], and then from a random sample on the manifold, the sample estimates are obtained and their properties like consistency and asymptotic distribution are examined ([7], [8], [6], [5]).

1.1 Research Approach and Contributions

In this study, two goals are pursued by definition of shape space,

-*Deformation interpolation*: During the deformation some samples are acquired from the object. However, to increase temporal resolution of the deformation, the interpolation seems to be inevitable. As the deformation samples are projected into shape space, the deformation becomes a curve in the highly dimensional shape space, which is called deformation path. Therefore, the problem of shape deformation interpolation is converted to interpolation of a curve on a high dimensional manifold, whose mathematical foundations are more developed. Furthermore, depending on the shape space, different interpolations are achieved.

-*Deformation classification*: Once the deformations are mapped into shape space, their geometrical differences which we are not interested in are removed. This makes them comparable as they are normalized in a common coordinate system. As a result, by comparison of the deformation paths on the shape space manifold, they can be classified easier than comparison of the original deformations in the 3D Euclidean space. This has applications in the classification of deformations such as the heart deformation. For instance, as opposed to the deformable models, one can classify the heart deformation just based on the geometrical information, without being aware of the underlying physical rules causing the deformation.

Towards these goals, first the desired topological and geometrical properties of an object are recognized to ease comparison and classification of the surfaces. This requires that a shape descriptor be defined. And then a metric is introduced regarding the characteristics of motions being studied. Although the shape descriptor captures the discriminating properties of objects, the similarity is a subjective issue. In the other word, one may prefer the topological properties as being more differentiating measures than minor visual differences. In the next two sections, the concepts of shape descriptor and metric will be reviewed briefly along with their characteristics.

1.1.1 Shape Descriptor

To extract the geometrical and topological information the shape descriptor is defined preserving the properties such as the transformations which the shape is invariant to. Thus the shape descriptors can be classified regarding to these transformation groups. Topological descriptors are global and less discriminating, yet the geometrical descriptors are local and more discriminating but need more storage, meaning they are computationally expensive. The shape descriptors should be as less sensitive as possible to the additive noise, and provide partial shape matching, i.e., only one part of the model information is compared to some other parts of other models. Three commonly used shape descriptor groups are,

-*Feature based shape descriptors*: These methods take into account only the pure geometry of the shape. Different features that these methods extract are global feature ([104], [20], [53]), global feature distribution ([74], [72]), spatial map ([2], [54], [71]), local feature ([85], [91], [60]).

-*Model graph shape descriptors*: These methods attempt to extract a geometric meaning from a 3D shape using a graph showing how shape components are linked together, e.g., model graphs [17], Reeb graphs ([90], [30]), and skeletons ([11], [39]).

-*View based shape descriptors*: If two models look alike from every angle they would be similar. The obvious application of these descriptors is to choose some 3D models based on their similarity to some 2D images. The distance between two descriptors is defined as the minimum L_1-difference, taken over all rotations ([29], [15]).

-*Deformation based shape descriptors*: In this descriptor the similarity is measured based on the deformation needed to register two shapes together. This descriptor can be used to define the evolution of a shape over time [4]. These shape descriptors are classified by the transformation groups, to which they are invariant.

The interested reader is referred to [92] to get more information on the shape descriptors.

1.1.2 Metric

Measuring the similarity of two objects necessitates definition of a similarity measure. If *d* is a similarity measure on a set **X**, then it should hold the following properties,

i. identity: $d\left(x,x\right)=0,\forall x\in$ **X**,

ii. positivity: $d\left(x,y\right)>0,\forall x,y\in$ **X**,

iii. symmetry: $d\left(x,y\right)=d\left(y,x\right),\forall x,y\in$ **X**,

iv. Triangle inequality: $d\left(x,z\right)\leq d\left(x,y\right)+d\left(y,z\right),\forall x,y,z\in$ **X**,

v. Transformation invariance: $d\left(g\left(x\right),g\left(y\right)\right)=d\left(x,y\right),\forall x,y,z\in$ **X** and $g\in$ **G**, where **G** is the desired transformation group.

Some of the above properties may not be met by some similarity measures but if all the properties are satisfied by a similarity measure, it is called a *metric*. The similarity measures obeying (*i*), (*iii*) and (*iv*) are called pseudo-metric and those satisfying (*i*), (*ii*) and (*iii*) are named semi-metric [96]. The similarity between two feature vectors is reflected in the distance between corresponding points in feature space [45]. Some commonly used metrics in the literature are,

1. L_p (Minkowski) distance: for two points x and y is defined as,

$$L_p\left(x,y\right)=\left(\sum_{i=0}^{N}\left|x_i-y_i\right|^2\right)^{\frac{1}{p}},\forall x,y\in\mathbb{R}^N.$$

2. *Hausdorff* distance: determines the distance between two point sets of different sizes. The directed Hausdorff distance is defined as,

$$\vec{h}\left(\mathbf{X},\mathbf{Y}\right)=\max_{x\in\mathbf{X}}\min_{y\in\mathbf{Y}}d\left(x,y\right),$$

where **X**, **Y** are two point sets. The final Hausdorff metric would be,

$$H\left(\mathbf{X},\mathbf{Y}\right)=\max\left[\vec{h}\left(\mathbf{X},\mathbf{Y}\right),\vec{h}\left(\mathbf{Y},\mathbf{X}\right)\right].$$

3. *Correlation* metric: determines the angle between two points in the feature space and is defined as follows,

$$C\left(\mathbf{X},\mathbf{Y}\right)=\frac{\sum_{i=0}^{N}\left(x_i-\bar{x}\right)\cdot\left(y_i-\bar{y}\right)}{\sqrt{\sum_{i=0}^{N}\left(x_i-\bar{x}\right)^2\cdot\sum_{i=0}^{N}\left(y_i-\bar{y}\right)^2}}.$$

As a deformation is shown by a curve in shape space, the length of the curve joining two points yields the similarity between two shapes according to the property which shape space preserves. Lipman et al. [62] estimate the deformation between two isometric manifolds by minimizing a geometric expressing functional. Huang et al. [41] suggest a constrained energy function based on the gradient domain techniques for deformation estimation. Zhou et al. [105] introduce the Volumetric Graph Laplacian technique to minimize a quadratic energy function preserving the volumetric details during the 3D deformation. Huang et al. [40] present a geometrical potential function with constant stiffness matrix to speed up the deformation approximation. Funck et al. [28] minimize an energy function based on the divergence free vector field to get a smooth, volume preserving deformation. Xu et al. [100] deal with the deformation as gradient field interpolation, and propose a novel shape interpolation approach based on the Poisson equation.

In contrast to the aforementioned methods, the geometric structure presented in [58] computes all smooth groups of diffeomorphisms mapping two objects together. The desired characteristics to which shape space is invariant can be induced by choosing an appropriate geometric structure. Completely invariant to the conformal transformations, a conformal structure based on the period matrix and related algorithms to calculate the period matrix for manifolds with arbitrary topologies are introduced in [35], [34]. Wang et al. [98] further provide a 3D matching framework based on the least squares conformal maps. In [102], a shape space is introduced to conformally map 2D smooth curves. To induce conformal mappings in 2D and quasi-conformal mappings in 3D, the Green Coordinates [63] are used in the cage-based space deformation estimation. Hurdal et al. [42] and Haker et al. [36] computed quasi-conformal and conformal maps of the cerebral cortex, respectively.

Continuous Ricci flow [37] conformally deforms a Riemannian metric on a smooth surface such that the Gaussian curvature evolves like a heat diffusion process. Eventually, the Gaussian curvature becomes constant and the limiting Riemannian metric is conformal to the original one. In discrete case, the circle packing metric [19] determines the discrete Gaussian curvature, and the discrete Ricci flow [48], [16] conformally deforms the circle packing metrics with respect to the Gaussian curvatures. In [50], the geodesic lengths of homotopy classes, measured by Hyperbolic Uniformization metric, is used to determine the coordinates of each conformal class in the Teichmüller shape space to classify the shapes with negative Euler number. In fact, surfaces with the same conformal class share the same Uniformization metric and can be used to classify the surfaces [49]. During the deformation, the Gaussian curvature at each point on the manifold may change according to the deformation characteristics. Based on the spectral geometry, the eigenvalues of the Laplace-Beltrami operator can serve as numerical fingerprints of 2D or 3D manifolds [77], which can also be used to build shape space invariant to isometric deformations.

1.2 Dissertation Organization

The following gives a brief description of the next chapters:

Chapter 2 explains the concept of shape space and different kinds of shape spaces in the literature.

Chapter 3 represents a new quasi-conformal metric based on the structure in [58]. This metric is employed to construct a new quasi-conformal shape space which can compare and differentiate different deformations. The heart anatomy and the conventional heart diagnostic methods such as ECG, Ultrasound, x-ray, are reviewed along with the conventional measures for the cardiac diagnosis. As of the goals of this study is to classify the deformation of the heart based on the geometrical information, we apply the proposed classification framework to classify the deformation of the left ventricle in some normal and abnormal subjects.

Chapter 4 presents a new shape space based on the medial surface. Indeed, the medial surface estimated the changes of the thickness of the shape, which is used as a valuable measure to diagnose the heart. Not only can this method classify the left ventricle deformation, but also it spots the abnormality on the abnormal left ventricle.

Chapter 5 draws a conclusion and explains the drawbacks of the proposed methods along with the future work.

CHAPTER 2

SHAPE SPACE

In this chapter, the concept of shape space as a non-linear Riemannian manifold and the proposed shape spaces in the literature are explained in details. Different shape spaces are categorized based on the transformation groups acting on them. Furthermore, the geodesic distance on each non-linear shape space manifold is measured by specific metrics which are compatible with the intrinsic geometry of the shape space manifold.

2.1 Introduction

The current shape analysis methods include analysis of the Cartesian coordinates of landmarks which preserve all the geometrical information and can be used to measure the shape features such as the angle between two vectors or the length of lines. Some basic geometric spaces used in the shape analysis are as follows:

1. *Landmark space* (figure space): Euclidean space in which landmarks are digitized and plotted.
2. *Configuration space* (form space): Euclidean Space in which landmark configurations are represented by single points (Fig. 2.1).
3. *Preshape space*: Non-Euclidean space in which configurations are plotted after scaling and translation.
4. *Shape space*: Non-Euclidean space in which configurations are plotted after the transformations preserving the intended geometrical properties. Thus, shape space has fewer dimensions than the configuration space. For instance, if we have k landmarks of m dimensions, in its corresponding similarity shape space,
    - 1 dimension lost in setting common scale.

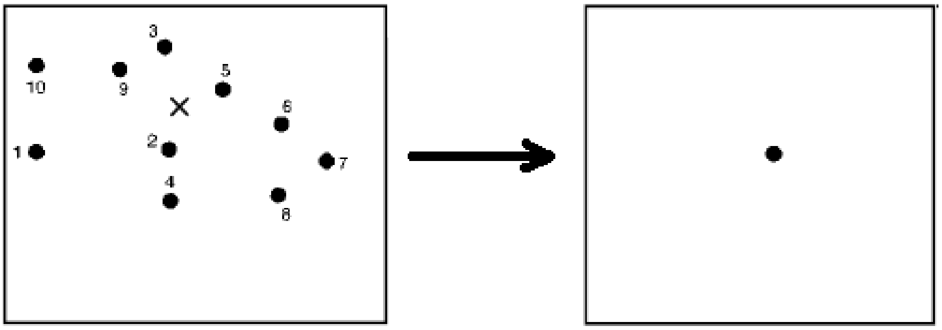

Figure 2.1: A 2D Landmark space (left) vs. its corresponding 20 (=2 × 10) dimensional Configuration space

- m dimensions lost in translating to common centers.
- $m(m-1)/2$ dimensions lost in rotation to common orientation.

Thus the dimensionality in shape space is $km - m - 1 - m(m-1)/2$.

5. *Tangent space*: Euclidean approximation of a shape space.

A shape metric describes the relationship between the distance in shape space and Euclidean distance in the original plane, which construct a Riemannian manifold [14]. The Hausdorff distance [43], the strain energy [82] and the Procrustes distance [22] are among the commonly used shape metrics.

2.2 Geometry of Shape Manifolds

Let (**M**, g) be a complete connected Riemannian manifold of dimension d with metric tensor g. Although some differentiable manifolds **M** exist as surfaces or hypersurfaces of the Euclidean space, e.g., a sphere $S^d = \{p \in \mathbb{R}^{d+1} : \|p\| = 1\}$, the shape space is not of this type of manifolds. Indeed, the shape space is a quotient space of a Riemannian manifold **N** under the action of a similarity transformation group **G**, i.e., $\mathbf{M} = \mathbf{N}/\mathbf{G}$. The intrinsic analysis on **M** makes use of the natural choice of the geodesic distance, in contrast with extrinsic analysis which maps **M** into the Euclidean space and computes the distance [38], [9].

The tangent space at a point p on **N** is decomposed into a vertical subspace V_p which is isomorphic to the tangent space of **G**, and a horizontal subspace H_p which is orthogonal to V_p and can be identified with the tangent space of **M**. Let **G** act as isometries of **N**, and $\pi : \mathbf{N} \longrightarrow \mathbf{M}$. Then, if $d\pi : T_p\mathbf{N} \longrightarrow T_{\pi(p)}\mathbf{M}$ is the differential of the projection π; then,

$$\langle d\pi\left(u\right), d\pi\left(v\right)\rangle_{\pi(p)} = \langle u, v\rangle_p ,$$

where $u, v \in T_p\mathbf{N}$.

2.3 Different Kinds of Shape Space

2.3.1 Similarity shape space and Kendall's Shape Space Σ_m^k

Consider a 2D or 3D configuration space having *k* landmarks. Its similarity shape is what remains after removing the effects of translation, scaling and rotation. The space of all similarity shapes forms the Similarity Shape Space Σ_m^k, where *m* is the dimension of the Euclidean space.

Kendall ([55], [56]) removed location and size differences between sets of point coordinates by centering each configuration on the origin and scaling each configuration to unit size as follows,

$$\mathbf{X'1} = \mathbf{0},$$

and

$$tr\left(\mathbf{XX'}\right) = \mathbf{1},$$

where size is defined as the sum of squared, Euclidean distances from each vertex to the corresponding vertex of the centriod configuration, **X** is a $k \times m$ matrix of the coordinates of *k* vertices in $\mathbb{R}^m$, **1** is a $p \times 1$ vector of 1's, and **0** a $k \times 1$ vector of 0's. The resulted configuration is called the preshape and lies in the unit sphere S_m^k. To remove differences due to special orthogonal rotations, the great circle distance *d* between each pair of configurations is minimized, which yields the geodesic distance on the shape space.

Assume $\pi : S_m^k \longrightarrow \Sigma_m^k$,

$$\rho\left(\pi\left(\mathbf{x}\right), \pi\left(\mathbf{x}\right)\right) = \inf_{\mathbf{R} \in SO(m)} d\left(\mathbf{R}\mathbf{x}, \mathbf{y}\right),$$

where $\mathbf{x}, \mathbf{y} \in S_m^k$, and ρ is the *Procrustes angular* (great circle) distance between the two shapes, which defines Kendall's shape space Σ_m^k of dimension $mk - m - 1 - m\left(m-1\right)/2$ which is a Riemannian manifold. Hence, $\Sigma_m^k = S_m^k / SO\left(m\right)$, $SO\left(m\right)$ is the group of $m \times m$ rotation matrices. The geodesic distance is the length of the great circle connecting **x** and **y** defined as,

$$d\left(\mathbf{x}, \mathbf{y}\right) = \arccos\left(tr\left(\mathbf{y}\mathbf{x}^T\right)\right).$$

In the special case of planar triangles, Σ_2^3 is isometric to the surface of a 2D sphere of radius 0.5 (Fig. 2.2). Kendall's development of shape theory is based on the Procrustes metric between pairs of configurations. An approach used in practical applications of shape analysis, is based on the least-squares superimposition, called Ordinary Procrustes Analysis.

Ordinary Procrustes Analysis (OPA)

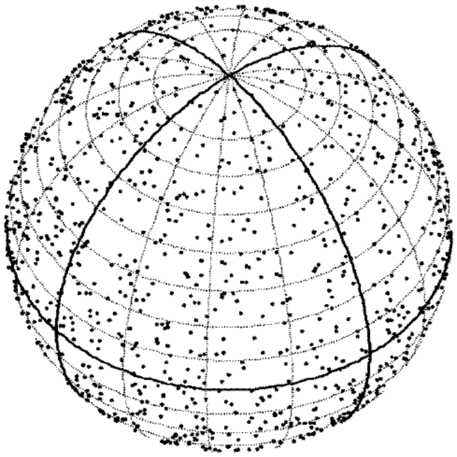

Figure 2.2: A view of Kendall's shape space for 2D triangles shows the mapping of some random triangles.

Let $\mathbf{X}_1$ and $\mathbf{X}_2$ be two k configurations, related to each other as,

$$\mathbf{X}_2 = \alpha \cdot (\mathbf{X}_1 + \mathbf{D}) \cdot \mathbf{R} + \mathbf{T},$$

Where α is a scale factor, $\mathbf{R} \in \mathbb{R}^{m \times m}$ is rotation matrix, $\mathbf{D} \in \mathbb{R}^{k \times m}$ is the matrix of shape difference between the two configurations, $\mathbf{T} \in \mathbb{R}^{k \times m}$ is the translation matrix. Now the translation and rotation matrices are calculated to minimize the sum of squared distances between corresponding vertices of $\mathbf{X}_1$ and $\mathbf{X}_2$, that's,

$$\mathbf{D}_P^2 = tr\left(\mathbf{D}\mathbf{D}^T\right),$$

where $\mathbf{D}_P$ is called Partial Procrustes distance. In [87], Slice shows that Procrustes superimposition does not lead to the Kendall's shape space, but to the surface of a hemisphere of radius 1 (Fig. 2.3). In the case of planar triangles, this space has a simple geometric relationship to Kendall's shape space.

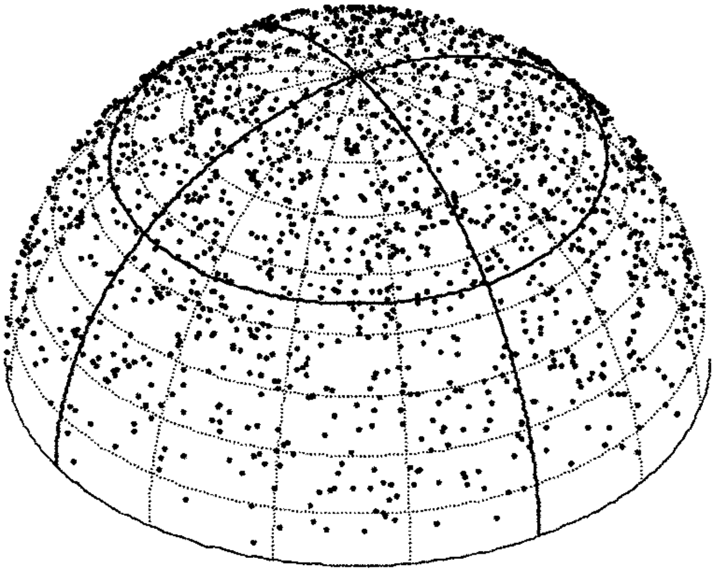

Figure 2.3: A view of the hemisphere of Procrustes-superimposed triangles representing the mapping of the triangles from Fig. 2.2.

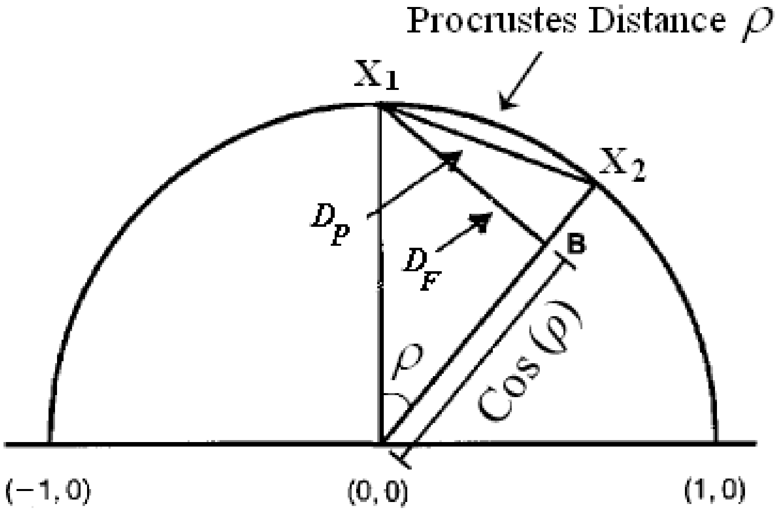

Figure 2.4: Procrustes distance (ρ) is not the shortest distance between two forms. Shorter distance is length of chord connecting two forms ($\mathbf{D}_P$). Shortest distance found by relaxing size constraint on one form, reducing to smaller centroid size in position B ($\mathbf{D}_F$).

In the kendall's shape space, each configuration is scaled to one (α=1), which does not minimize $\mathbf{D}_P$, in contrast, here different values are assigned to α to minimize $\mathbf{D}_P$. It is shown that $\alpha = \cos(\rho)$ minimizes $\mathbf{D}_P$. which is called *full Procrustes distance* ($\mathbf{D}_F$) (Fig. 2.4).

2.3.2 Planar Shape Space Σ_2^k

A 2D configuration space having k landmarks can be presented on a complex plane as $\{z_j = x_j + iy_j, 1 \leq j \leq k\}$. The location, size and orientation differences are removed as,

$$\{\lambda \cdot (z_j - \bar{z}), 1 \leq j \leq k\},$$

$$\bar{z} = \frac{1}{k} \cdot \sum_{j=1}^{k} z_j,$$

where $\lambda = re^{i\theta}$, and r is the scaling factor and θ is the rotation angle. Each configuration is a complex line passing through $\bar{z}$. The planar shape space is the set of complex lines in $\mathbb{C}^{k-1}$ passing through origin, which has the structure of the complex projective space $\mathbb{C}P^{k-2}$.

Assume

$$u = \left\{ \frac{(z_j - \bar{z})}{\|z_j - \bar{z}\|}, 1 \leq j \leq k \right\},$$

is the preshape of the configuration, which lies on the $\mathbb{C}S^{k-1}$, where

$$\mathbb{C}S^{k-1} = \left\{ u \in \mathbb{C}^k : \sum_{j=1}^{k} u_j = 0, \|u\| = 1 \right\}.$$

Then the mapping $\pi : \mathbb{C}S^{k-1} \to \Sigma_2^k$ is as follows,

$$\pi(u) = \left\{ e^{i\theta} u, -\pi \leq \theta \leq \pi \right\},$$

which is a curve on the unit sphere $\mathbb{C}S^{k-1}$. The geodesic distance in the planar shape space is as follows,

$$\rho(\pi(u), \pi(v)) = \inf_{\theta \in (-\pi, \pi]} d\left(u, e^{i\theta} v\right),$$

where $u, v \in \mathbb{C}S^{k-1}$, and d is the geodesic distance on $\mathbb{C}S^{k-1}$,

$$d(u, v) = \arccos\left(Re\left(\bar{v}^T u\right)\right).$$

One can determine the distance between two preshapes u and v by trying to minimize the Euclidean distance between them as rotate one of them, that's,

$$d_P(u, v) = \min_{\theta \in (-\pi, \pi]} \left\| u - e^{i\theta} v \right\|,$$

d_P is the Partial Procrustes distance on the planar shape space.

2.3.3 Reflection shape space $R\Sigma_m^k$

Let $\mathbf{X} \in \mathbb{R}^{k \times m}$ be a k configuration and $z \in S_m^k$ be its preshape after centering each configuration on the origin and scaling to unit size. The Reflection shape space of z is as follows,

$$\sigma\left(z\right)=\left\{\mathbf{A}z:\mathbf{A}\in O\left(m\right)\right\},$$

where $O\left(m\right)$ is the group of $m\times m$ orthogonal matrices. For the set of nonsingular $z\in S_m^k$, $R\Sigma_m^k=S_m^k/O\left(m\right)$ is a Riemannian manifold of dimension $mk-m-1-m\left(m-1\right)/2$.

As aforementioned, $\Sigma_m^k=S_m^k/SO\left(m\right)$. Therefore, $R\Sigma_m^k=\Sigma_m^k/\mathbf{G}$, where $\mathbf{G}$ is the group of reflections which maps a configuration to its reflected configuration. Therefore, the similarity shape space Σ_m^k and the reflection shape space $R\Sigma_m^k$ have the same Riemannian metric as they are locally alike.

The geodesic distance between two preshapes $u,v\in S_m^k$ is as follows,

$$\rho\left(\pi\left(u\right),\pi\left(v\right)\right)=\inf_{\mathbf{F}\in O(m)}d\left(u,\mathbf{F}v\right),$$

where

$$d\left(u,v\right)=\arccos\left(tr\left(uv^T\right)\right).$$

The full procrustes distance is,

$$d_F\left(u,v\right)=\inf_{\alpha\in\mathbb{R}^+,\mathbf{F}\in O(m)}\left\|u-\alpha\mathbf{F}v\right\|.$$

It is proven that the infimum is achieved [59],

$$d_F\left(u,v\right)=\left[1-\left(\sum_{i=1}^{m}\lambda_i\right)^2\right]^{\frac{1}{2}},$$

where λ_i is is the i^{th} eigenvalue of the matrix uv^T. Accordingly, the partial procrustes distance is,

$$d_P\left(u,v\right)=\inf_{\mathbf{F}\in O(m)}\left\|u-\mathbf{F}v\right\|.$$

It is proven that the infimum is achieved,

$$d_P(u,v) = \sqrt{2}\left[1 - \sum_{i=1}^{m} \lambda_i\right]^{\frac{1}{2}}.$$

2.3.4 Affine shape space $A\Sigma_m^k$

The orbit of the configuration space under affine transformations constructs the affine shape space, $A\Sigma_m^k$,

$$A\Sigma_m^k = \left\{\sigma(x), x \in \mathbb{R}^{m\times k}\right\},$$

where

$$\sigma(x) = \{\mathbf{A}x + \mathbf{b} : \mathbf{A} \in GL(m,\mathbb{R}), \mathbf{b} \in \mathbb{R}^m\},$$

$GL(m,\mathbb{R})$ is the general linear group in $\mathbb{R}^m$ of all $m \times m$ nonsingular matrices.

Two centered configurations $x, y \in \mathbb{R}^{m\times k}$ correspond by a non-singular transformation, i.e., $(y - \bar{y}) = \mathbf{A}(x - \bar{x})$. The subspace of the centered configurations is $\mathbb{H}(m,k)$ which is a Euclidean manifold of dimension $m(k-1)$; therefore, the affine shape space is the quotient of this space under the general linear transformations, i.e., $A\Sigma_m^k = \mathbb{H}(m,k)/GL(m,\mathbb{R})$ having $m(k-1) - m^2$ dimensions.

2.3.5 Projective Shape Space

All the lines in $\mathbb{R}^{m+1}$ passing through the origin constitute the real projective space $\mathbb{R}P^m$. The elements of $\mathbb{R}P^m$ are presented as,

$$[x] = \{\lambda x : \lambda \neq 0\},$$

where $x \in \mathbb{R}^{m+1}\ \{0\}$.

The projective transformation α in $\mathbb{R}P^m$ is $\alpha[x] = [\mathbf{A}x]$, $A \in GL(m+1,\mathbb{R})$. The group of all projective transformations is $PGL(m)$.

As each line passing through the origin can be represented by its intersection points with the unit sphere S^m, $\mathbb{R}P^m = S^m/\mathbf{G}$, where **G** contains both identity and antipodal maps. The geodesic distance between $[u], [v] \in \mathbb{R}P^m$ where $u, v \in S^m$ is,

$$\rho([u],[v]) = \min\left[d(u,v), d(u,-v)\right],$$

where $d(u,v) = \arccos\left(u^T v\right)$. As a result, the projective shape of a *k* configuration is,

$$\alpha(x) = \left\{(\alpha[x_1], \cdots, \alpha[x_k]) : \alpha \in PGL(m), x_i \in \mathbb{R}^{m+1}, k > m+2\right\}.$$

A *projective frame* is an ordered set of *m*+2 points in $\mathbb{R}P^m$ which is in *general position*, that's, their linear span is in $\mathbb{R}P^m$. Let $\mathbf{G}(m,k)$ denote the set of all ordered systems of *k* points $p_1, \cdots, p_k$ for which $p_1, \cdots, p_{m+2}$ is a projective frame. The shape of all *k* configurations in general position is the projective shape space $P\Sigma_m^k$; therefore, $P\Sigma_m^k = \mathbf{G}(m,k)/PGL(m)$. It is proven in [65] that there is a diffeomorphism between $P\Sigma_m^k$ and a product of real projective spaces $(\mathbb{R}P^m)^{k-m-2}$.

2.3.6 Isometric shape space

As a non-rigid object deforms over time, the corresponding points in shape space form a curve on the shape space manifold, called *deformation path* (Fig. 2.5).

Depending on the geometrical property which the shape space is invariant to, different deformation paths can be achieved. Here, we are interested in the isometric deformations, that's, the lengths of edges are preserved during the deformations.

Let $\mathbb{G}$ be the space of all immersions having a fixed connectivity in 3D Euclidean space, and $\mathbf{M} \in \mathbb{G}$ be an immersion at time *t*, which contains *N* vertices, thus **M** is a vector in $\mathbb{R}^{3N}$. Since **M** deforms smoothly, the deformation path at the vertex $p \in \mathbf{M}$ is a continuously differentiable function, $\mathbf{f}_p(t) : [0,1] \to \mathbb{R}^3$, and the deformation function of **M** is $\mathbf{f}(t) : [0,1] \to \mathbb{R}^{3N}$. Let $T_M\mathbb{G}$ be the tangent space of $\mathbb{G}$ at the point **M**. Thus $\mathbf{X} \in T_M\mathbb{G}$ assigns a deformation vector

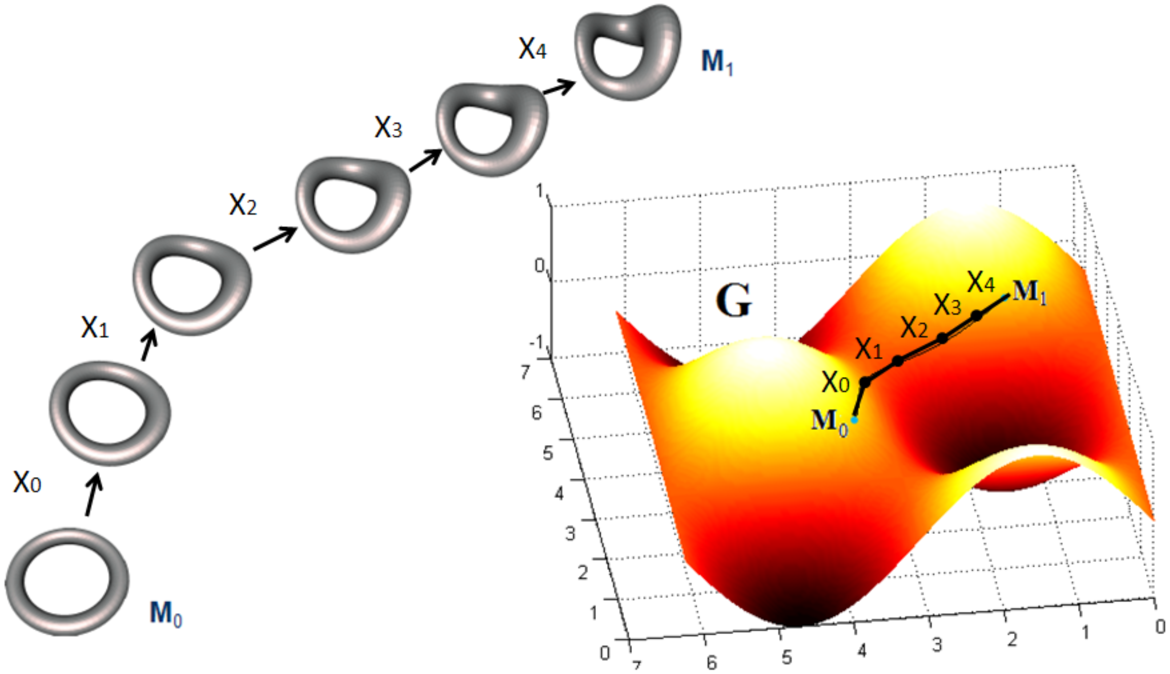

Figure 2.5: The shape deformation corresponds to a curve on the shape space manifold.

$X_p(t) = \partial p(t)/\partial t$ to every vertex p at time t. Here we define an *as Isometric as possible* space, which does not impose strict isometricity on the deformation, in contrast, it discourages non-isometricity of the deformation. As mentioned, the edge length is constant during the deformation,

$$\|p(t) - q(t)\|^2 = Const,$$

where (p, q) is an edge on **M**; therefore,

$$\frac{\partial \|p(t) - q(t)\|^2}{\partial t} = 0 \Rightarrow \langle \mathbf{X}_p - \mathbf{X}_q, p - q \rangle = 0,$$

where $\langle \cdot, \cdot \rangle$ is the canonical inner product in $\mathbb{R}^3$.

The norm of the deformation field **X** on the mesh **M** is a measure of non-isometricity of the deformation,

$$\|\mathbf{X}\|_M^I = \sum_{(p,q)\in M} \langle \mathbf{X}_p - \mathbf{X}_q, p-q\rangle^2 ,$$

which shows the distance between two poses of the shape at two time points. The final metric is defined as the inner product of two vectors fields **X** and **Y** on the tangent space of $\mathbb{G}$,

$$\langle\langle \mathbf{X}, \mathbf{Y}\rangle\rangle_M^I = \sum_{(p,q)\in M} \langle \mathbf{X}_p - \mathbf{X}_q, p-q\rangle \cdot \langle \mathbf{Y}_p - \mathbf{Y}_q, p-q\rangle .$$

This is a symmetric and bilinear function which defines a semi-Riemannian metric on $\mathbb{G}$ [58]. [99] proposes a shape space approximating the most isometric model by linearly interpolating in shape space.

2.3.7 Rigid-body shape space

A deformation is Rigid body if the following relation holds for the deformation field $\mathbf{X}(t)$,

$$\mathbf{X}_p(t) = k_1(t) + k_2(t) \times p(t) ,$$

Where $k_1(t)$ and $k_2(t)$ are some smoothly varying vector in $\mathbb{R}^3$. As in the Kendall's shape space, the Rigid-body component of the deformation is extracted from the whole deformation by minimizing the following functional,

$$\min_{k_1,k_2} \sum_{p\in M} \langle \mathbf{X}_p(t) - k_1(t) - k_2(t) \times p(t) , \mathbf{X}_p(t) - k_1(t) - k_2(t) \times p(t)\rangle . \tag{2.1}$$

If $\hat{k}_1(t)$ and $\hat{k}_2(t)$ minimize Eq. 2.1, the Rigid body metric is defined as,

$$\langle\langle \mathbf{X}, \mathbf{Y}\rangle\rangle_M^R = \sum_{p\in M} \left\langle \mathbf{X}_p(t) - \hat{k}_1(t) - \hat{k}_2(t) \times p(t) , \mathbf{Y}_p(t) - \hat{k}_1(t) - \hat{k}_2(t) \times p(t) \right\rangle .$$

which is a linear and symmetric real valued function [58].

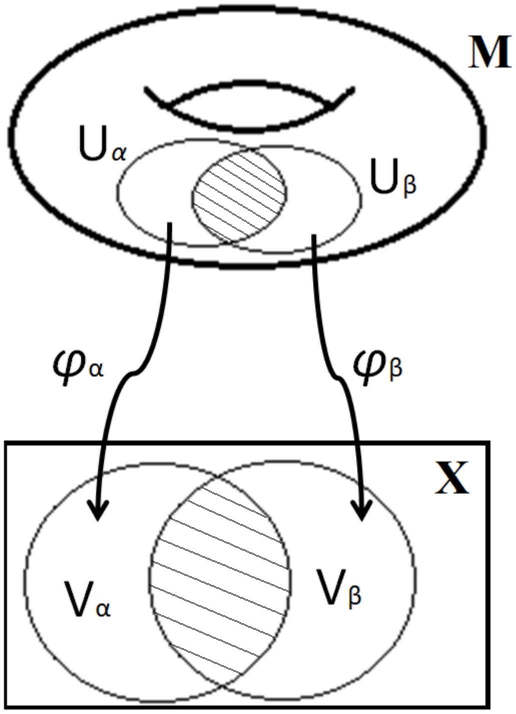

Figure 2.6: A chart is a homeomorphism from a neighborhood on the manifold **M** to another neighborhood on the simple topological space **X**, which is called the local coordinate on **X**

2.3.8 Conformal map

In a simply connected surface any closed curve is the full boundary of some portion of the surface (The Riemann sphere, the finite complex plane, the unit disk), in contrast with a multiply connected surface which doesn't hold this property (annulus) [59].

If **M** is a real, *n*-dimensional topological manifold, each point $p \in \mathbf{M}$ has an open neighborhood U_α for which we can find a homeomorphism $\varphi_\alpha : U_\alpha \to V_\alpha$ to an open ball V_α in a simple space **X** such as the Euclidean space. Such a homeomorphism is called a *coordinate chart* around *p*. A collection of charts which cover the manifold is called an *atlas*, $A = \{(U_\alpha, \varphi_\alpha)\}$ (Fig. 2.6).

Charts may overlap such that a portion of the manifold is mapped by different charts. A *transition function* $T_{\alpha\beta} : \mathbf{X} \to \mathbf{X}$ maps an open ball V_α to V_β, where they overlap in **X**, that's, $T_{\alpha\beta}(v) = \varphi_\beta \circ \varphi_\alpha^{-1}(v)$ where $v \in \{V_\alpha \cap V_\beta\}$. The (**X**, **G**) is a structure on the surface **M**, where **G** is the group of all transition functions. For instance, a spherical structure contains the local coordinates on the sphere along with all rotation functions as the transition functions.

The atlas might contain a collection of maps from **M** to the Euclidean space. If the Euclidean plane is identified with the complex plane, the topological atlas is a *complex atlas*, and the corresponding structure is called the *complex structure*. A complex function $f : (x, y) \rightarrow (u, v)$ which satisfies the Riemann-Cauchy equation,

$$\frac{\partial u}{\partial y} = -\frac{\partial v}{\partial x}, \frac{\partial u}{\partial x} = \frac{\partial v}{\partial y},$$

is called a *holomorphic* function. A surface **M**, whose all transitions functions being holomorphic is called *Riemannian surface*, and its atlas is called *conformal atlas*. The maximal conformal atlas is *conformal structure* of **M**. Let $\mathbf{M}_1$ and $\mathbf{M}_2$ be two Riemannian surfaces whose local charts are φ_α and ψ_β, respectively, and $\tau : \mathbf{M}_1 \rightarrow \mathbf{M}_1$ be a mapping between two surfaces. If the mapping is always holomorphic, τ is called *holomorphic map* or *conformal map*. A conformal map between two surfaces preserves the angles between curves on the surface, and a conformal structure measures the angle [33].

2.3.9 Teichmüller shape space

Surfaces are conformally equivalent, if they can be conformally mapped to each other. All conformally equivalent shapes constitute a conformal class. Each conformal class is assigned one point in the Teichmüller shape space. Let **M** be a real, *n*-dimensional topological manifold, $S(\mathbf{M})$ be the set of all complex structures of **M**, and $x_0 \in \mathbf{M}$. The set of continuous functions are called loops with the base point x_0, $\mathbf{L}(\mathbf{M}, x_0)$. The fundamental group of **M** with base point x_0, $\pi(\mathbf{M}, x_0)$ is,

$$\pi(\mathbf{M}, x_0) = \mathbf{L}(\mathbf{M}, x_0) / h,$$

where *h* is the set of homotopy function of $\mathbf{L}(\mathbf{M}, x_0)$. Therefore, the fundamental group contains the loops going around holes and handles and their combinations (Fig. 2.7).

Definition: $PSL(2, \mathbb{C})$ is a group of isometries of the hyperbolic plane, which acts on the

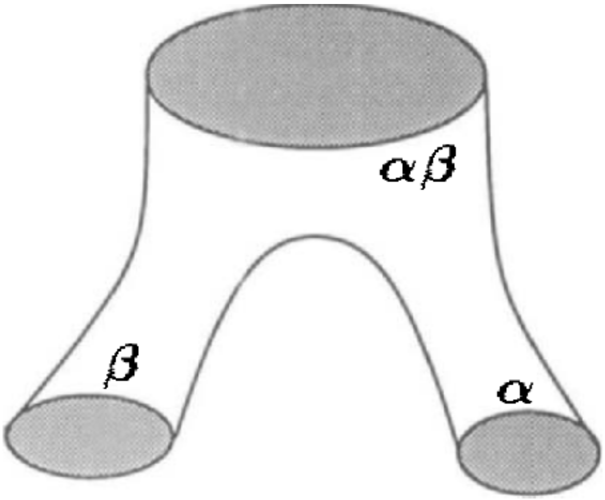

Figure 2.7: A pair of pants and its fundamental group containing three homotopy classes $\{\alpha, \beta, \alpha\beta\}$.

upper half plane by möbius transformations,

$$\begin{pmatrix} a & b \\ c & d \end{pmatrix} \cdot z = \frac{az+b}{cz+d}.$$

Definition: Let $\mathbf{G} \subset PSL\left(2, \mathbb{C}\right)$ act invariantly on an open disk $\mathbf{D} \subset \hat{\mathbb{C}}$, that is, $\mathbf{G}\left(\mathbf{D}\right) = \mathbf{D}$. Then $\mathbf{G}$ is Fuchsian group if and only if,

1. $\mathbf{G}$ is a discrete group,
2. $\mathbf{G}$ acts properly discontinuously at each point $z \in \mathbf{D}$,
3. The set $\mathbf{D}$ is a subset of the region of discontinuity of $\mathbf{G}$.

The corresponding Fuchsian group $\mathbf{G}$ generated by möbius transformations is isomorphic to $\pi\left(\mathbf{M}, x_0\right)$, that's,

$$i : \pi\left(\mathbf{M}, x_0\right) \rightarrow \mathbf{G},$$

where $i\left(\langle\alpha\rangle\right) = g$, $i\left(\langle\beta\rangle\right) = h$, and $i\left(\langle\alpha\beta\rangle\right) = g \circ h$. These möbius transformations cover the homotopy class of curves going around the handles and holes, and $logk\left(g\right)$, $logk\left(h\right)$, and

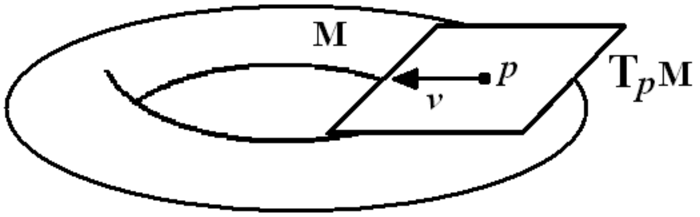

Figure 2.8: The tangent space at a point *p* is the set of velocity vectors of all possible curves passing through the point *p* on the manifold **M**.

$logk\left(g\circ h\right)$ are the lengths of the geodesic loops in the homotopic classes. $k\left(g\right)$, $k\left(h\right)$, and $k\left(g\circ h\right)$ are the multipliers of the möbius transformations.

Now the Teichmüller shape space, $T\left(\mathbf{M}\right)$, is constructed as the set of the lengths of all geodesic loops, e.g.,

$$T\left(\mathbf{M}\right)=\left\{k\left(g\right),k\left(h\right),k\left(g\circ h\right)\right\},$$

thus the Teichmüller space of the pair of pants is in $\mathbb{R}^3_+$.

2.4 Tangent Space

The tangent space $T_p\mathbf{M}$ at a point $p\in\mathbf{M}$ is the set of velocity vectors of all possible curves passing through the point *p* on the manifold **M**. The collection of all tangent vectors to every point on the manifold, called the *tangent bundle*. If $\varphi:V_\alpha\to V_\beta$ is a diffeomorphism between two charts, the tangent vector *v* at the point $q\in V_\alpha$ is considered as a tangent vector $\mathbf{J}_\varphi v$ at the point $\varphi\left(q\right)\in V_\beta$, where $\mathbf{J}_\varphi v$ is the Jacobian matrix which represents a linear transformation. Therefore, the tangent space is independent of the chart (Fig. 2.8).

2.4.1 Linearization of shape space

Since shape space is non-Euclidean, linear statistical procedures cannot be applied on such spaces. To make the shape space linear, the shape space in a neighborhood can be projected onto the tangent space ($\mathbf{P}:\mathbf{G}\to T_M\mathbb{G}$). For instance, there are three projection methods in the Kendall's shape space (Fig. 2.9).

1. *Orthogonal projection*: The point $\mathbf{N}\in U_M$ is projected onto the tangent plane, that's,

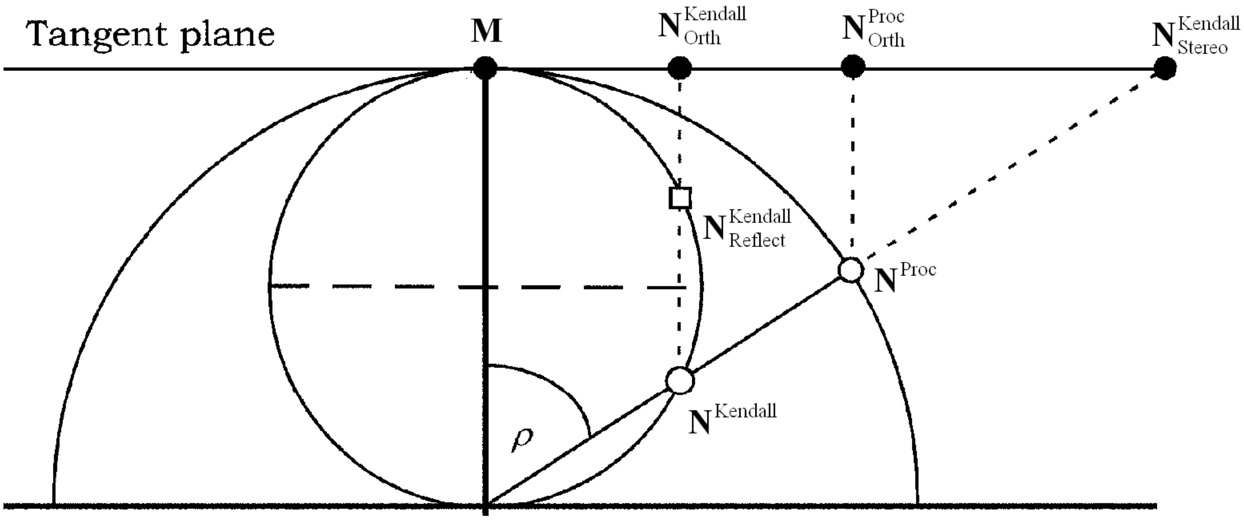

Figure 2.9: The geometric relationship between the Procrustes hemisphere and Kendall's shape space for tangent space projections.

$\mathbf{P}\left(\mathbf{N}^{Kendall}\right) = N^{Kendall}_{Orth} \in T_M\mathbb{G}$. However, the points on both sides of the equator of the Kendall's sphere are mapped to the same point on the tangent plane, that's,

$$\mathbf{P}\left(\mathbf{N}^{Kendall}\right) = \mathbf{P}\left(\mathbf{N}^{Kendall}_{Reflect}\right) = N^{Kendall}_{Orth}.$$

2. *Stereographic projection*: In this method, the south pole of the sphere is the reference point of the stereographic projection, that's, $\mathbf{P}\left(\mathbf{N}^{Kendall}\right) = N^{Kendall}_{Stereo} \in T_M\mathbb{G}$.

3. *Orthogonal projection on the Procrustes hemisphere*: In this method, the corresponding point on the Procrustes hemisphere (N^{Proc}) is orthogonally mapped onto the tangent plane ($\mathbf{P}\left(\mathbf{N}^{Proc}\right) = N^{Proc}_{Orth}$), which is a unique, one-to-one mapping of points to a unit disk.

It is shown that the third projection method provides better approximation of the distance in the Kendall's shape space than the others [79].

CHAPTER 3

QUASI-CONFORMAL DEFORMATION CLASSIFICATION IN SHAPE SPACE

In order to classify a group of shapes, some geometrical or topological features are extracted, and the shapes are classified based on the extracted features. During the deformation of an object, its corresponding point in shape space will follow a non-linear curve on the shape space manifold. The distance between two points in shape space determines the dissimilarity of their corresponding shapes, regarding the geometrical property the shape space is invariant to. This makes the shape space a useful tool to classify different deformations based on the intended geometrical property.

3.1 Introduction

This chapter presents a novel approach based on the shape space concept to classify deformations of 3D models. In our method, a novel quasi-conformal metric is introduced which measures the curvature changes at each vertex of the simplicial complex during the deformation. The deformation curve is obtained by minimizing an energy function to find the geodesic curve connecting two shapes in the shape space manifold. The proposed classification framework is very effective for the analysis of the intrinsic geometric changes of the shapes in shape space. Our contributions in this chapter can be summarized as follows,

- we propose a novel framework for the effective analysis of dynamic shapes and shape deformations in a low dimensional shape space,
- we propose a novel quasi-conformal metric to characterize and classify the quasi-conformal deformations in shape space.
- We applied our classification framework on the left ventricle deformations. The experi-

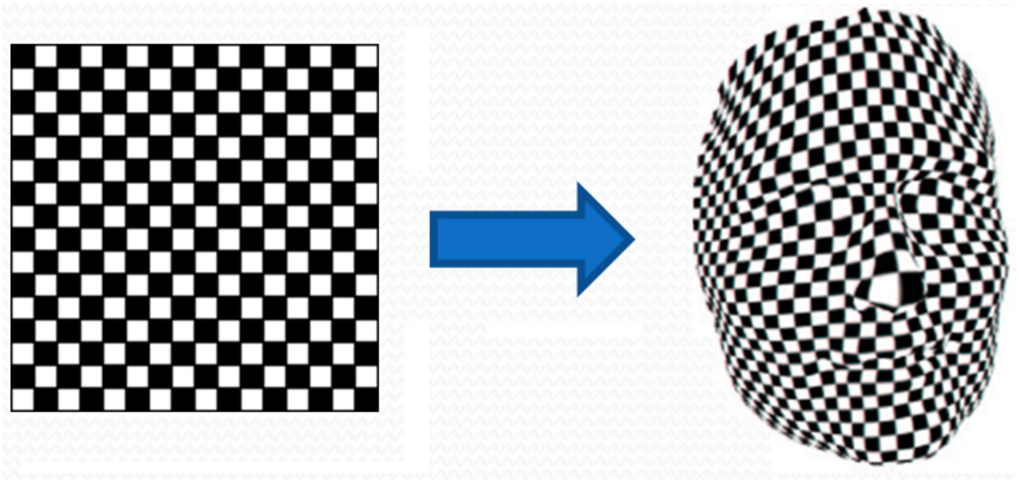

Figure 3.1: The conformal map preserves the angle between the perpendicular lines on the chessboard when maps the chessboard to the face.

mental results show that our proposed metric can build a shape space which is compatible with the intrinsic geometrical characteristics of the left ventricle deformation.

3.2 Conformal and Quasi-conformal metrics

Let Σ be a simplicial complex, and a mapping $f : \Sigma \rightarrow \mathbb{R}^3$ embed Σ to the Euclidean space, then $\mathbf{M} = (\Sigma, f)$ is a triangular mesh. Let the vertices $\{p, q, r\}$ be three vertices of the face Δpqr of **M** and $\{X_p, X_q, X_r\}$ be their corresponding deformations.

In the Riemannian geometry, each metric is defined as the inner product of two vector fields. Suppose two different deformation fields as **X** and **Y**, the distance between them are measured by $\langle\langle \mathbf{X}, \mathbf{Y} \rangle\rangle$ in shape space. Based on the Riemannian metric definition, two conformal and quasi-conformal metrics are proposed to construct the appropriate shape space.

3.2.1 Conformal metric

During the conformal deformation, the angle between two edges of each triangle will be preserved (Fig. 3.1).

Let Δpqr and $\Delta \acute{p}\acute{q}\acute{r}$ be two triangles such that,

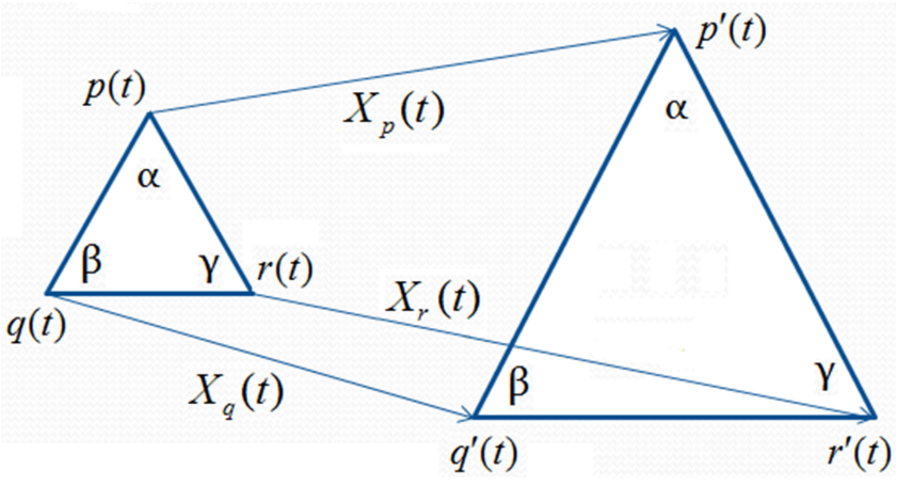

Figure 3.2: The triangle on left is deformed to the triangle on right and the corresponding angles are the same during the deformation.

$$\begin{cases} \acute{p}(t) = p(t + \Delta t) = p(t) + X_p(t) \\ \acute{q}(t) = q(t + \Delta t) = q(t) + X_q(t) \\ \acute{r}(t) = r(t + \Delta t) = r(t) + X_r(t) \end{cases}$$

In the Euclidean geometry, if the edge lengths of a triangle are multiplied by the same coefficient, the resulting triangle would have the same angles as the original one (Fig. 3.2). Generalizing this idea, we try to preserve the proportion of two edge lengths of each triangle during the deformation,

$$\frac{\|\acute{p}(t) - \acute{q}(t)\|^2}{\|p(t) - q(t)\|^2} = \frac{\|\acute{p}(t) - \acute{r}(t)\|^2}{\|p(t) - r(t)\|^2}. \tag{3.1}$$

Eq.3.1 yields the following relation,

$$\frac{\|\acute{p}(t) - \acute{q}(t)\|^2 - \|p(t) - q(t)\|^2}{\|p(t) - q(t)\|^2} = \frac{\|\acute{p}(t) - \acute{r}(t)\|^2 - \|p(t) - r(t)\|^2}{\|p(t) - r(t)\|^2} \Rightarrow$$

$$\frac{\|p(t+\Delta t) - q(t+\Delta t)\|^2 - \|p(t) - q(t)\|^2}{\|p(t) - q(t)\|^2} = \frac{\|p(t+\Delta t) - r(t+\Delta t)\|^2 - \|p(t) - r(t)\|^2}{\|p(t) - r(t)\|^2}.$$

The numerator shows the changes of the squared edge length within Δt. If $\Delta t \to 0$; then, the numerator will be equal to the derivative of the squared edge length, that's,

$$\lim_{\Delta t \to 0} \frac{\|p(t+\Delta t) - q(t+\Delta t)\|^2 - \|p(t) - q(t)\|^2}{\Delta t \cdot \|p(t) - q(t)\|^2} = \lim_{\Delta t \to 0} \frac{\|p(t+\Delta t) - r(t+\Delta t)\|^2 - \|p(t) - r(t)\|^2}{\Delta t \cdot \|p(t) - r(t)\|^2} \Rightarrow$$

$$\frac{1}{\|p(t) - q(t)\|^2} \cdot \lim_{\Delta t \to 0} \frac{\|p(t+\Delta t) - q(t+\Delta t)\|^2 - \|p(t) - q(t)\|^2}{\Delta t} = \frac{1}{\|p(t) - r(t)\|^2} \cdot \lim_{\Delta t \to 0} \frac{\|p(t+\Delta t) - r(t+\Delta t)\|^2 - \|p(t) - r(t)\|^2}{\Delta t} \Rightarrow$$

$$\frac{1}{\|p(t) - q(t)\|^2} \cdot \frac{\partial \|p(t) - q(t)\|^2}{\partial t} = \frac{1}{\|p(t) - r(t)\|^2} \cdot \frac{\partial \|p(t) - r(t)\|^2}{\partial t}.$$

By differentiating $\|p(t) - q(t)\|^2$ and $\|p(t) - r(t)\|^2$, Eq.3.2 will be derived,

$$\frac{\langle p(t) - q(t), X_p(t) - X_q(t) \rangle}{\|p(t) - q(t)\|^2} = \frac{\langle p(t) - r(t), X_p(t) - X_r(t) \rangle}{\|p(t) - r(t)\|^2}. \tag{3.2}$$

Now the conformal part of the deformation can be defined as,

$$T_p(\mathbf{X}) = \langle p(t) - q(t), X_p - X_q \rangle \cdot \|p(t) - r(t)\|^2 - \langle p(t) - r(t), X_p - X_r \rangle \cdot \|p(t) - q(t)\|^2 . \tag{3.3}$$

Likewise, $T_q(\mathbf{X})$ and $T_r(\mathbf{X})$ are calculated. To preserve angles of each triangle Δpqr, a similarity transformation requires that all $T_p(\mathbf{X})$, $T_q(\mathbf{X})$ and $T_r(\mathbf{X})$ vanish during deformation, thus the following metric is obtained for the conformal deformations.

$$T_{\Delta pqr}(\mathbf{X}) = |T_p(\mathbf{X})| + |T_q(\mathbf{X})| + |T_r(\mathbf{X})| .$$

Finally the *Angle Preserving* metric can be achieved as,

$$\langle\langle \mathbf{X}, \mathbf{Y} \rangle\rangle^{AP}_{\mathbf{M}} = \sum_{\Delta pqr \in \mathbf{M}} T_{\Delta pqr}(\mathbf{X}) \cdot T_{\Delta pqr}(\mathbf{Y}). \tag{3.4}$$

Indeed, this metric takes out the conformal part of the deformation and measures the distance between two shapes based on the non-conformal part of the deformation.

3.2.2 Quasi-conformal metric (an improvement on the angle-preserving metric)

Although the current metrics can measure the characteristics of many kinds of deformations, there are still more non-conformal deformations for which we are interested to define a shape space, whose geometry more accurately reconciles to the characteristics of these non-conformal deformations. For instance, during the heart deformation, one part of the heart expands while the other portion contracts, meaning the heart deformation is not conformal in the strict sense. This necessitates a quasi-conformal shape space which better preserves these non-conformal deformation characteristics.

To produce the quasi-conformal metric, we take the changes of the curvature at each vertex into account such that a vertex with lower change in curvature has less effect in the final value of the metric. Let K_p be the curvature at vertex p before deformation. The curvature of an interior vertex can be approximated as,

$$K_p = 2\pi - \sum_{\Delta pqr \in \mathbf{M}} \theta_p^{qr},$$

If the vertex is a boundary vertex the curvature is,

$$K_p = \pi - \sum_{\Delta pqr \in \mathbf{M}} \theta_p^{qr},$$

where, θ_p^{qr} is the corner angle attached to the face Δpqr and can be achieved by the *cosine law* depending on the background geometry. If the edge lengths satisfy the triangle inequality,

$\|p-q\| + \|q-r\| > \|p-r\|$, then the corner angle θ_p^{qr} is calculated as,

$$\|q-r\|^2 = \|q-p\|^2 + \|p-r\|^2 - 2\,\|q-p\|^2 \cdot \|p-r\|^2 \cdot \cos\left(\theta_p^{qr}\right).$$

Now the conformal part of the deformation which takes into account the changes in the local curvature is as follows,

$$\tilde{T}_p(\mathbf{X}) = \Delta K_p \cdot \left[\langle p-q, X_p - X_q\rangle \cdot \|p-r\|^2 - \langle p-r, X_p - X_r\rangle \cdot \|p-q\|^2\right],$$

Likewise, the values of $\tilde{T}_q(\mathbf{X})$ and $\tilde{T}_r(\mathbf{X})$ are calculated. As in the conformal metric,

$$\tilde{T}_{\Delta pqr}(\mathbf{X}) = \left|\tilde{T}_p(\mathbf{X})\right| + \left|\tilde{T}_q(\mathbf{X})\right| + \left|\tilde{T}_r(\mathbf{X})\right|.$$

Finally the quasi-conformal metric is,

$$\langle\langle \mathbf{X}, \mathbf{Y}\rangle\rangle_{\mathbf{M}}^{QC} = \sum_{\Delta pqr \in \mathbf{M}} \tilde{T}_{\Delta pqr}(\mathbf{X}) \cdot \tilde{T}_{\Delta pqr}(\mathbf{Y}). \tag{3.5}$$

In this way, not only are the changes of the curvature of each vertex measured, but also the complexity of the final metric would be reduced.

3.2.3 Energy optimization

To find the shortest path connecting two points on a manifold, the integral of the first fundamental form of the manifold is minimized.

$$E(\mathbf{M}) = \int \langle\langle \mathbf{X}, \mathbf{X}\rangle\rangle_{\mathbf{M}}\, dt.$$

In a triangular mesh, the summation of the edge lengths connecting two vertices are mini-

Figure 3.3: The main pipeline of the classification framework.

mized, which yields the following energy function [58],

$$E(\mathbf{M}) = \sum_{i} \left(\langle\langle \mathbf{X}_i, \mathbf{X}_i \rangle\rangle_{\mathbf{M}_i} + \langle\langle \mathbf{X}_i, \mathbf{X}_i \rangle\rangle_{\mathbf{M}_{i+1}} \right),$$

where $\mathbf{M}_i$ is the i^{th} vertex of the polygon inscribed on the curve and $\mathbf{X}_i$ is the i^{th} edge of the polygon. The intermediate vertices of the polygon are changed to minimize the energy function.

3.3 The Deformation Analysis Framework

Based on the shape deformation an algorithm is proposed to classify the deformation of shapes. Fig. 3.3 shows the pipeline of our algorithm. In first step, we find the best rigid alignments of the triangular meshes at sequential time points. The more accurate the rigid alignment, the more accurate the deformation classification is. The following describes the rest of the pipeline in details.

3.3.1 Temporal Interpolation

To estimate the deformation of an object some time-varying samples should be taken from the object during the deformation. In some scenarios, the temporal sampling might not be satisfactory. In order to improve the temporal resolution of the sampling, the interpolation step is necessary. The algorithm to interpolate the deformation is as follows.

Suppose two sequential meshes $\mathbf{M}_i$ and $\mathbf{M}_{i+1}$ represented by two sequential points on the deformation curve in shape space and $\mathbf{P}_i$ is the i^{th} intermediate mesh. The average point of the pair of points is considered as an initial intermediate point. Then by minimizing the energy functional $E(\mathbf{M})$, the intermediate point is determined more accurately reflecting the applied

```
Input: Initial meshes $\mathbf{M}_i$ and $\mathbf{M}_{i+1}$
Output: Interpolated meshes $\{\mathbf{P}_1, ..., \mathbf{P}_n\}$
$\mathbf{M} \leftarrow \{\mathbf{M}_i, (\mathbf{M}_i + \mathbf{M}_{i+1})/2, \mathbf{M}_{i+1}\}$;
while Number of intermediate meshes is reached do
    $\{\mathbf{P}_1, ..., \mathbf{P}_n\} \leftarrow argminE(\mathbf{M})$;
    $\mathbf{M} \leftarrow \{\mathbf{M}_i, (\mathbf{M}_i + \mathbf{P}_1)/2, \mathbf{P}_1, ..., \mathbf{P}_n, \mathbf{M}_{i+1}\}$;
end
```

metric. In the next step, some other initial intermediate points may be entered to the energy functional and all the intermediate meshes will be finally optimized together. As mentioned in [58], some other consideration may be taken into account to speed up the optimization procedure and find the local minimum quickly. In our framework, a multiresolution approach is employed. For instance, we use the coarse meshes as initial meshes, and the local minimum search is achieved quickly in this case. Then, the vertices of these coarse meshes will work as initial vertices for other finer meshes. Thus, the intermediate refined meshes can be obtained more reliably in this way, rather than having problems to optimize high resolution intermediate meshes, which may take long time to complete.

3.3.2 Deformation Transfer

Two deformations are comparable, if their deformation curves are transferred to the same part of shape space. In the Euclidean shape space, this is simple and will not change the curve, but in non-Euclidean shape space, the *parallel transport* approach is employed for the deformation transfer (Fig. 3.4).

Let $\mathbf{M}$ be an immersion on the shape space manifold $\mathbb{G}$. We sample the deformation path at equidistant points $\mathbf{M}_i$, thus the line segments connecting each pair of sequential samples will be $X_i = \Delta\mathbf{M}_i$ (i.e., a discrete tangent vector). The deformation of $\mathbf{M}$ is transferred to the point $\mathbf{N}_0$ such that $\mathbf{M}_0$ is mapped to $\mathbf{N}_0$.

Let the curve $\gamma_0 : [0\ 1] \rightarrow \mathbb{G}$ be the geodesic line on the shape space manifold connecting $\mathbf{M}_0 = \gamma_0(0)$ to $\mathbf{N}_0 = \gamma_0(1)$, and $X_0(t)$ be a vector field along γ_0 at time *t*. $X_0(t)$ is called *parallel* if the angle $\alpha_0 = \langle\langle X_0(t), \gamma_0'(t)\rangle\rangle_{\gamma_0(t)}$ is constant, provided $X_0(t)$ rotates minimally

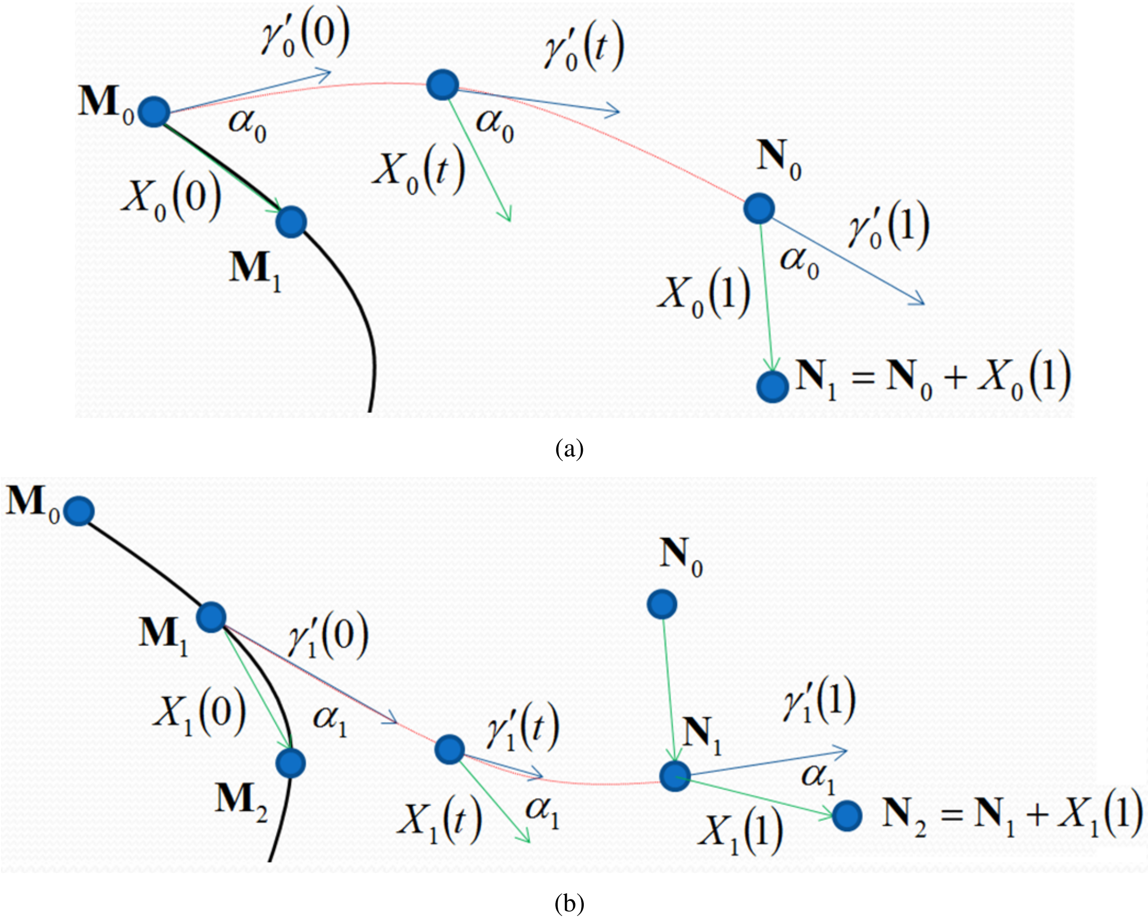

Figure 3.4: The deformations should be transferred to the same part of shape space using Parallel Transport approach; otherwise, they are not comparable. Here, the deformation $\mathbf{M}$ is transferred to the point $\mathbf{N}_0$ along the geodesics on the manifold. (a)The first step, $\mathbf{M}_1$ is transferred to $\mathbf{N}_1$, (b) the second step, $\mathbf{M}_2$ is transferred to $\mathbf{N}_2$.

around $\gamma_0'(t)$. We take some samples along γ_0 and calculate $X_0(t)$ at the discrete time points as follows,

$$\min_{\bar{X}} \left\| \bar{X} - X_0(t_i) \right\|^2 ,$$

subject to:

$$\alpha_0 = \langle\langle \bar{X}, \gamma_0'(t_{i+1}) \rangle\rangle_{\gamma_0(t_{i+1})} ,$$

Where $\bar{X}$ yields $X_0(t_{i+1})$. Once $X_0(t)$ is transferred along γ_0, $N_1 = N_0 + X_0(1)$ is achieved

(Fig. 3.4.a).

In the second step, the geodesic line γ_1 connecting $\mathbf{M}_1$ to $\mathbf{N}_1$ is calculated and the vector $X_1(0)$ is transferred along it to achieve $X_1(1)$ and $N_2 = N_1 + X_1(1)$ (Fig. 3.4.b). We keep transferring deformation segments until all the segments are transferred [58].

3.3.3 Dimension Reduction

At this point, all deformation paths have been transferred to the same part in shape space. But high dimensional shape space prohibits an intuitive perception of deformation comparison. As a result, redundant dimensions of shape space should be eliminated such that the projected deformation paths are as similar as possible to the original deformation paths. Some methods such as PCA, Factor Analysis and ICA are low cost linear methods but they can not reveal the geometry of shape space, due to non-linearity of the shape space manifold.

In some other dimension reduction methods such as Multidimensional scaling, Isomap, Locally Linear Embedding, a non-linear cost function is minimized to extract the most informative dimensions. These methods are more likely to fulfill the needs of shape space, since they minimize a non-linear cost function which better estimates the main features on a non-

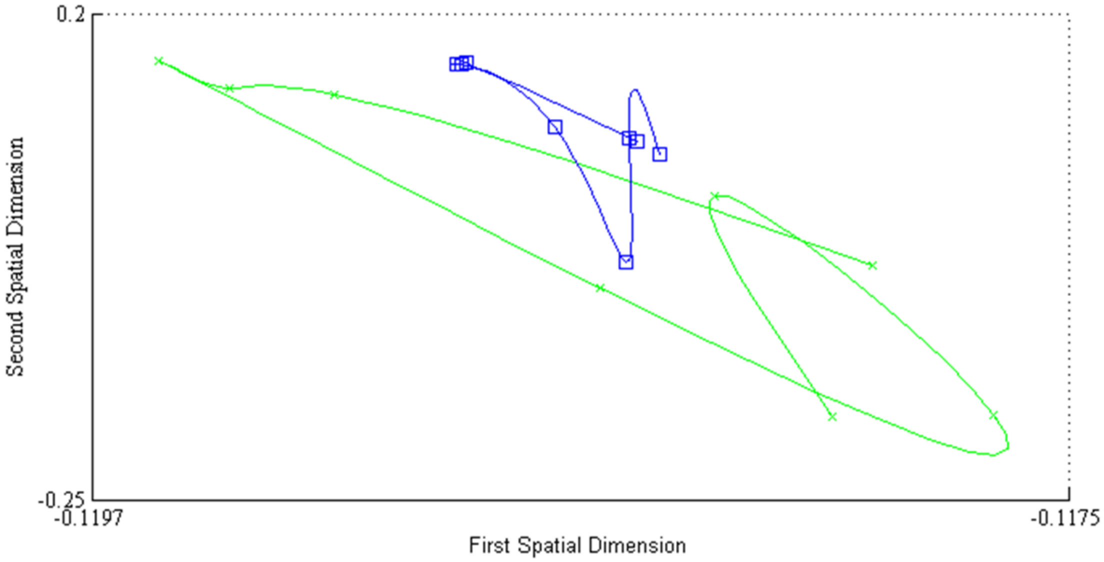

Figure 3.5: Two deformation paths projected on the 2D spatial space after being transferred to the same part of the shape space.

linear shape space manifold. Towards this end, a distance matrix demonstrating distance of each pair of meshes is built based on the defined metric. Then, the *MultiDimensional Scaling* (MDS) method is employed to reduce dimensions of shape space and project deformation paths onto a 2D space, called the *2D spatial space*. Fig. 3.5 illustrates two deformation paths after being projected on the 2D spatial space. On the 2D plane, one can better perceive the similarity between them.

3.3.4 Deformation Classification

Although deformations take place in time but we do not have any consideration about time in this deformation structure. To address this issue, time is added to the 2D spatial space, as the third dimension. We call this new 3D shape space, *spatiotemporal space*. Finally, the *Locally Linear Embedding* (LLE) method is used to map 3D deformation curves onto a 2D plane such that each point in this 2D plane corresponds to one deformation curve in the spatiotemporal space. The more similar two deformations, the closer their corresponding points are in the 2D plane. By adding time as the third dimension to the 2D spatial space rather than to the original shape space, time would have more effect in the final deformation projection process as a naturally different dimension.

Fig. 3.6.a illustrates two deformation paths in the 3D spatiotemporal space. Although, the two deformations look different in the 3D space but their similarity is revealed when they are projected onto the 2D plane which is constituted by one of the spatial dimensions and time. Indeed, the deformations follow the same pattern which could not been recognized in the spatiotemporal space (Fig. 3.6.b).

3.4 Experiments on Synthetic Datasets

Some genus zero and one models are deformed in accordance with different deformation patterns, thus the point correspondence between consecutive poses is known beforehand. Different experiments on the synthetic datasets evaluate its performance on deformation classification and its resistance against additive noises.

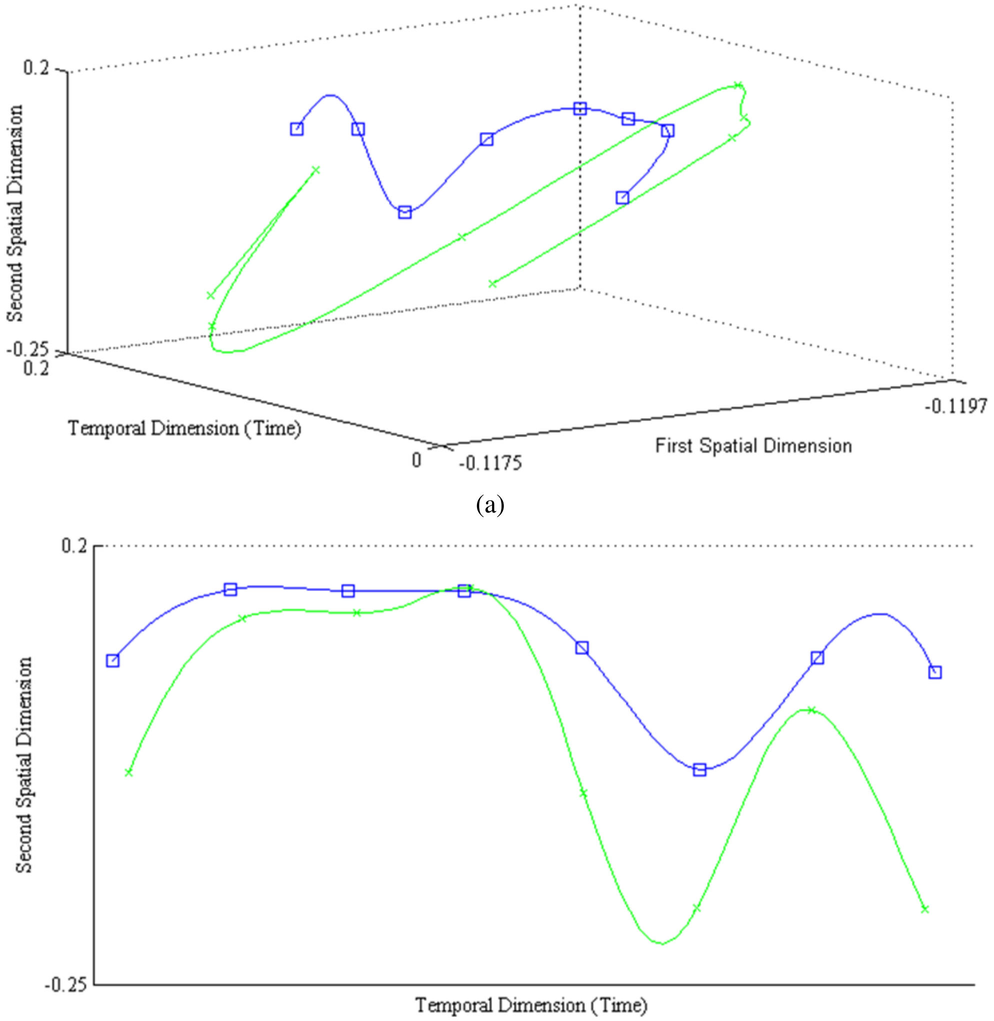

(a)

(b)

Figure 3.6: Two deformation paths are (a) in the 3D spatiotemporal space projected, (b) The two deformations projected onto the 2D plane.

3.4.1 Shape Interpolation

Two poses of the models serve as input poses and the intermediate poses are interpolated by the aforementioned algorithm. Fig. 3.7 shows the deformations of a torus and a sphere, which are interpolated using the proposed metric. The leftmost and rightmost poses in each row are the input poses, and three intermediate poses are the interpolated poses. As seen in Fig. 3.7.c and d, only the upper hemisphere deforms during the deformation and the lower part is still. Therefore, the upper part has more effect on the final energy functional as its curvature changes more than that of the lower part. In other words, the upper hemisphere accounts for the geodesic distance of the sequential poses in shape space more than the lower hemisphere.

3.4.2 Deformation Transfer

To have different deformations comparable in shape space, their deformations are transferred to the same part of shape space. Towards this end, some models are deformed non-conformally; and then, their deformations are transferred to other models. The more accurately the non-conformal deformations are followed by the second model without distortion, the better the metric can estimate the intrinsic geometry of shape space and preserve the invariant characteristics of the models during deformation. Fig. 3.8.a and c demonstrates two non-conformal deformations of a sphere and a torus, which are followed by an ellipsoid (Fig. 3.8.b) and a deformed torus (Fig. 3.8.d), respectively.

Although the sphere deforms non-conformally, the ellipsoid can accurately follow the de-

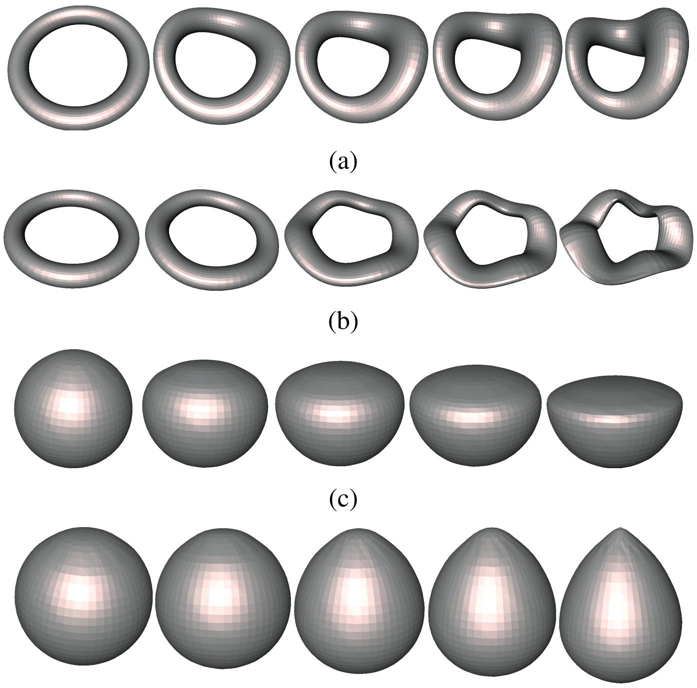

(a)

(b)

(c)

(d)

Figure 3.7: The interpolation of a-b) a torus and c-d) a sphere deformation using the metric. Two poses at two ends of each row are the input poses and the middle poses are the interpolated ones.

formation, and the quasi-conformal metric can circumvent the local minima during optimization of the energy functional by learning the geometry of shape space. We applied the deformation transfer method based on our metric on 60 deformations, all of which were successfully followed by different objects.

3.4.3 Deformation Classification

In the next step, some different deformations are applied on a torus and classified by the classification algorithm. Since we classify the synthetic datasets, the corresponding points on different meshes are known. Fig. 3.9 illustrates classification of different deformations of

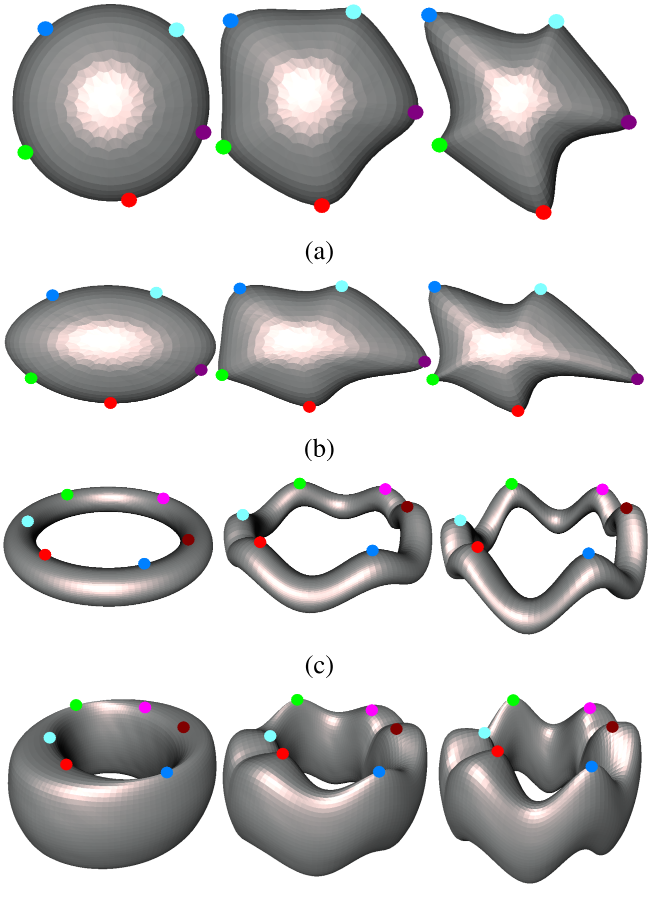

Figure 3.8: a) The non-conformal deformations of a) a sphere and c) a torus within three time points from left to right, which are followed by b) an ellipsoid and d) a deformed torus, respectively. The leftmost poses in the figures (b) and (d) are the input poses following the deformations in (a) and (c).

a torus, in which only the representative deformations are shown next to solid dots, and the deformations corresponding to the soft dots are not depicted due of lack of space. As seen, the similar deformations will be close together in the 2D plane.

3.4.4 Noise Resistance

Due to the acquisition procedures, some datasets might contain some noise, thus one aspect of classification is about how accurately a classifier can classify noisy datasets. To evaluate this, the points corresponding to different deformations in the 2D plane are classified into some classes by the k-means clustering algorithm. Let $\mathbf{K}$ be the set of all points corresponding to all deformations and $\mathbf{k}_i$ be the set of points classified in the group i^{th} by the k-means method. In addition, let k_i belong to the set $\mathbf{k}_i$, and l_i be its assigned label. Eq.3.6 calculates the statistic τ quantifying the performance of the algorithm as follows,

$$\tau = \frac{\sum_i |\{k_i \in \mathbf{k}_i \mid l_i = i\}|}{|\mathbf{K}|} \ . \tag{3.6}$$

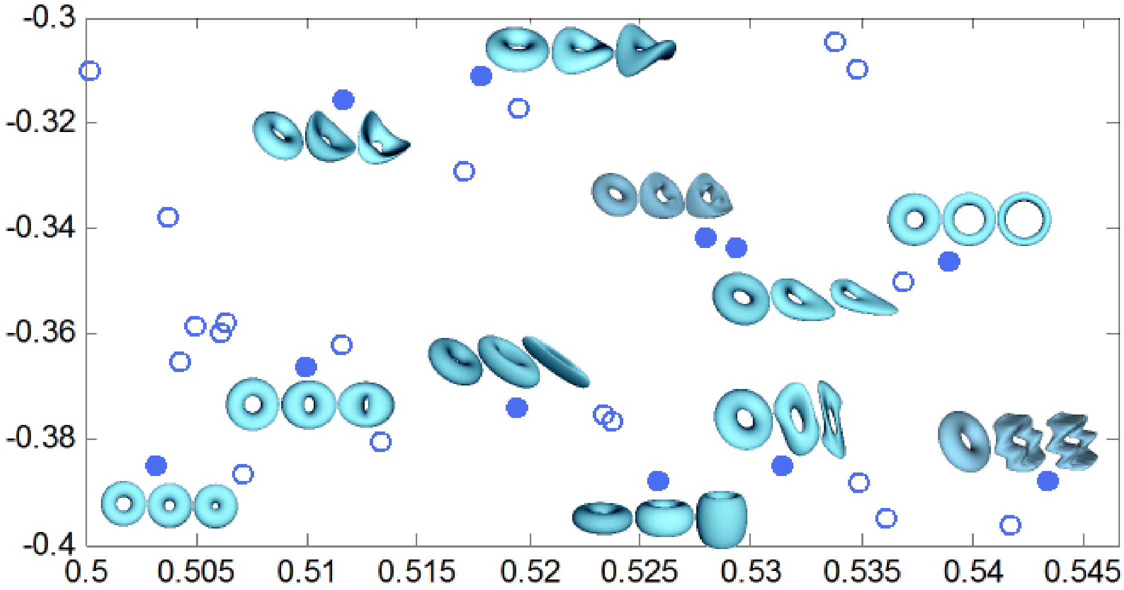

Figure 3.9: The classification of different deformations applied on a torus such that each dot corresponds to one deformation (Two axes are first and second coordinates of LLE). Each deformation is illustrated by three poses at three consecutive time points, the leftmost pose is the initial pose and the two right poses are the next sequential poses.

Table 3.1: Performance of the algorithm against noisy datasets with different percentages of additive noise variance

Noise Variance	Uniform Noise	Gaussian Noise	Poisson Noise
1%	99.6%	99.4%	99.2%
2.5%	99.3%	97.3%	97.2%
5%	96.0%	94.4%	95.1%
10%	90.1%	88.8%	89.0%
20%	74.7%	72.9%	73.2%

Table 3.1 represents the algorithm performance against additive noises with different distributions, which were added to the synthetic genus zero or one meshes with zero, one or two boundaries. As can be seen, the percentage of misclassified deformations is acceptable up to 10% of additive noise, meaning the pattern of deformations of topologically different meshes can be detected well. Besides the algorithm shows better performance against the uniform noise compared with the noise with either Gaussian or Poisson distribution.

3.5 The Application of Shape Space Techniques for Functional Analysis of Cardiac Images

The Cardiovascular Disease (CVD) is the number one cause of death in the United States [26]. There are some information acquisition techniques available to understand cardiac motions and their relationship to CVD. The heart has four chambers, the right atrium (RA), right ventricle (RV), left atrium (LA), and left ventricle (LV), whose functions are to pump blood throughout the body [Fig. 3.10].

In this section, some conventional heart diagnostic techniques are introduced along with some cardiac imaging techniques. Then, the classification of the left ventricle deformation is carried out using the proposed quasi-conformal shape space.

3.5.1 Eectrocardiogram(ECG)

The electrocardiogram (ECG or EKG) is a diagnostic tool that measures the electrical activity of the heart (Fig. 3.11). By interpretation of the ECG signals, cardiologists can diagnose different cardiovascular diseases, such as supraventricle arrhythmias, ventricle arrhythmias, atrial enlargement (hypertrophy), ventricular enlargement (hypertrophy), myocardial ischemia and infarction, and so on.

The electrical activity results in P, QRS, and T waves, which show a wide range of abnormalities of both the electrical conduction system and the muscle tissue of the chambers. How-

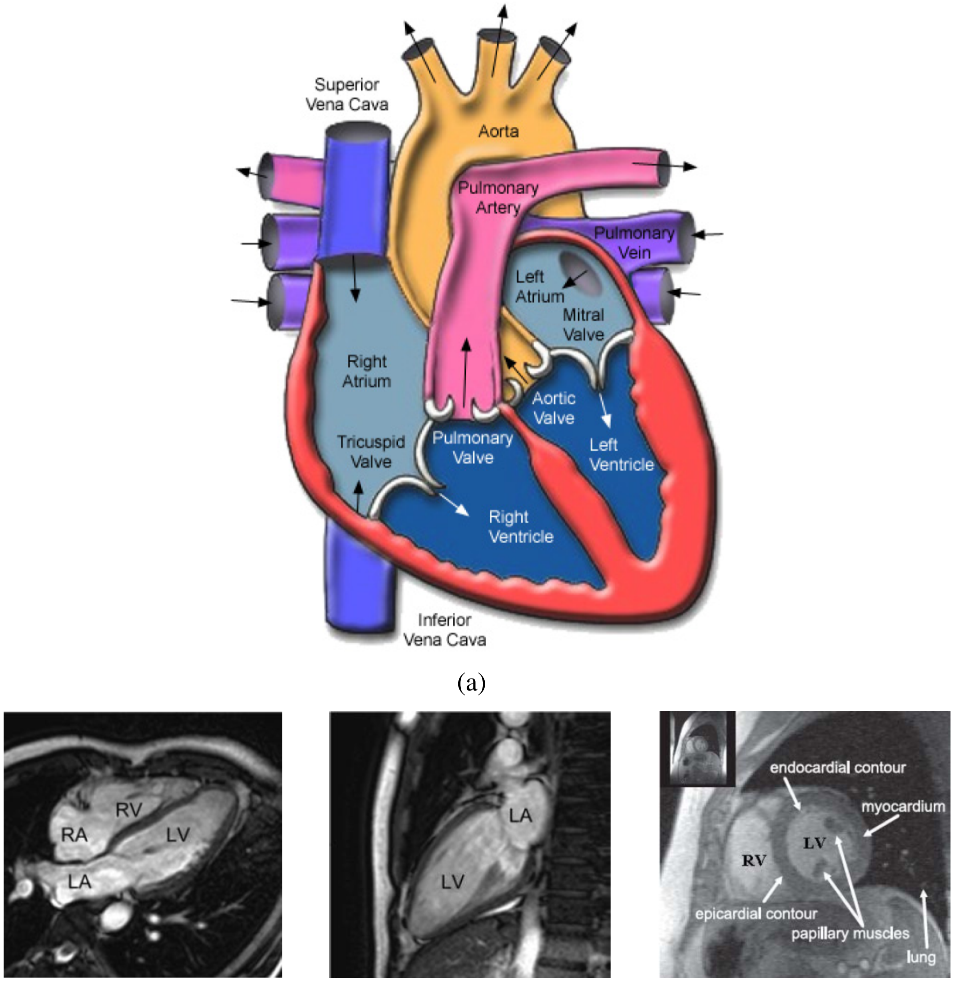

(a)

(b)

Figure 3.10: (a) Diagram of the heart, (b) The MRI images of the heart in the three axial, coronal, and sagital views.

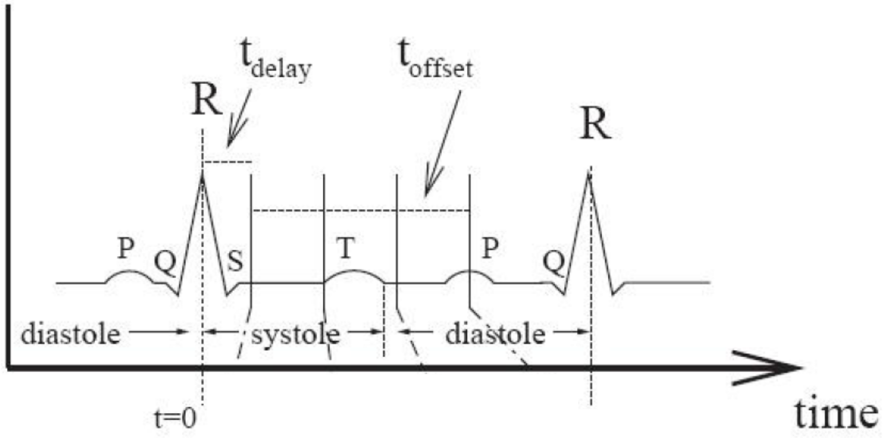

Figure 3.11: Form of ECG signal.

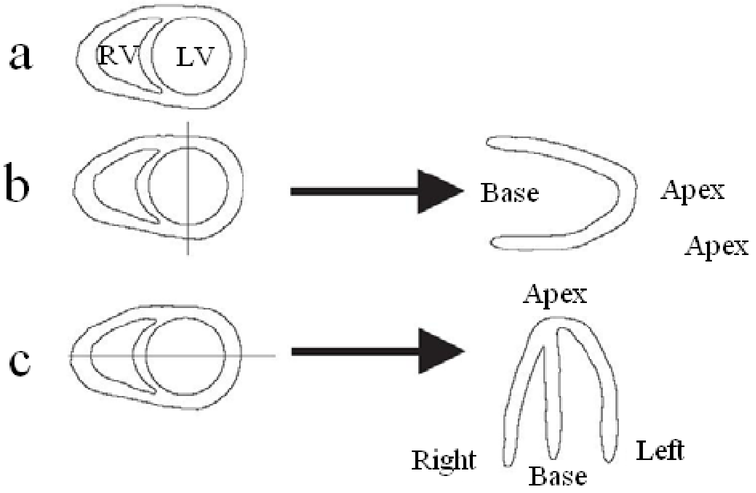

Figure 3.12: This schematic represents the heart in the chest. The slices are illustrated in (a) the short axis view, (b) the vertical long axis view, (c) the horizontal long axis view.

ever, the interpretation of the ECG signals needs to be verified with other diagnostic methods.

3.5.2 Cardiac Axis

In the cardiac imaging techniques the heart is shown from three different views (Fig. 3.12),

1. *Short Axis* (*SA*): Short Axis images cut through the left ventricle from the apex to the base,
2. *Vertical Long Axis* (*VLA*): Vertical Long images cut the left ventricle from the septal wall

to the lateral wall,

3. *Horizontal Long Axis* (*HLA*): Horizontal Long images cut through the left ventricle from the posterior wall to the anterior wall.

3.5.3 Heart image acquisition techniques

- *Angiocardiography*: First a contrast medium is injected and guided to the lesion to be enhanced by placing a catheter, and then the X-ray image of the heart is acquired (Fig. 3.13). Angiocardiography is usually good at anatomic delineation of lesions and to assess ejection fraction (EF) based on simplified geometric models of the LV [57].

-*Cardiac Ultrasound*: Some pulsed ultrasound waves are applied on the body over the skin, and their echo with respect to blood velocity and direction of flow is mapped over the 2D or 3D image [70]. This technique reveals the anatomy and movement of the heart non-invasively (Fig. 3.14).

-*Isotope Imaging*: This technique is mostly used to study ejection fraction [31], regional wall motion analysis of the left ventricle [25]. There are two types of Isotope imaging. 1. first-pass studies: The first passage of the injected contrast through the heart is illustrated by 2D images, 2. gated equilibrium studies: the tracer mixed with the blood before data collection is shown by 2D or 3D images (Fig. 3.15).

Figure 3.13: The angiocardiography image of the heart vessels.

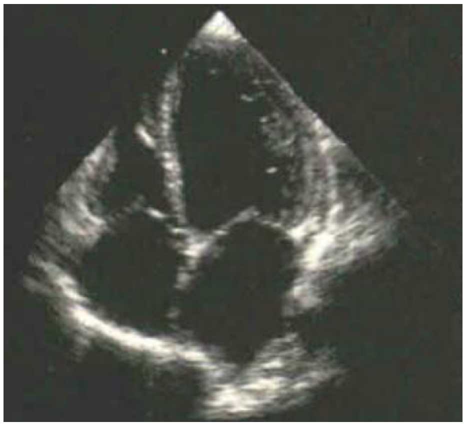

Figure 3.14: The four chambers of the heart are illustrated in the cardiac ultrasound image of the heart.

-*Cardiac CT*: Spiral CT, ultrafast CT are used for cardiac CT imaging, which produce real time multiple cross sections, 3D images of cardiac chambers, and information on coronary calcium deposits [73] (Fig. 3.16).

-*Cardiac MRI*: MRI is vastly used to extract the anatomical and functional information of the RV and LV [64], wall-thickening, myocardial motion, and circumferential shortening of myocardial fibers [67]. MRI is capable of acquiring multiple imaging planes with high soft tissue contrast between the blood and myocardium non-invasively. The Tagged-MRI technique is used to track the myocardium deformation over time (Fig. 3.17).

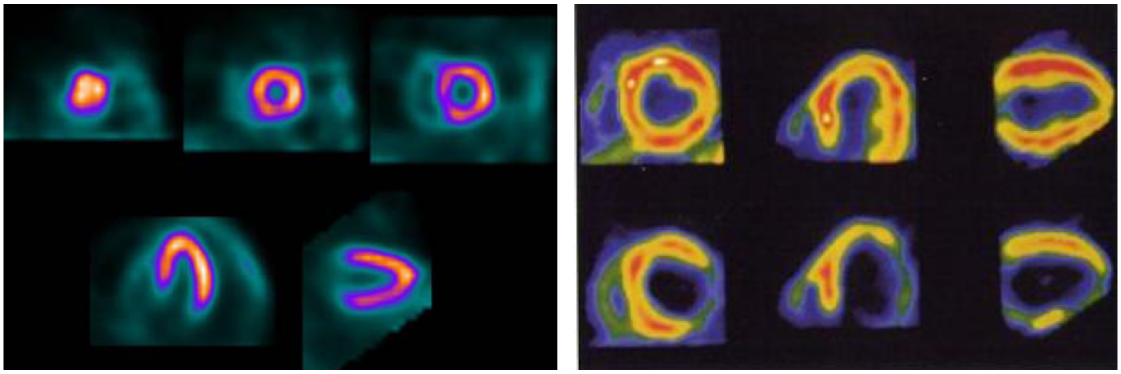

Figure 3.15: The isotope image of the left ventricle.

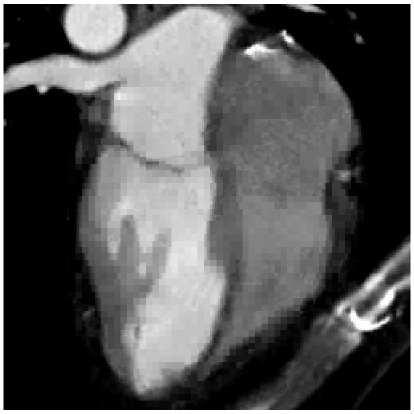

Figure 3.16: The CT image of the heart.

3.6 Experimental Results

As aforementioned, the Electrocardiogram (ECG) is a bioelectrical signal recording the electrophysiological behavior of the heart over time. By interpretation of the ECG signal, the cardiologist can diagnose various heart diseases.

However, in most cases the cardiac diagnosis needs to be verified with other diagnostic methods like x-ray, coronary angiography, radiocardiographic imaging, ultrasound, and so on. In these methods, the cardiologists diagnose the heart using some 2D images, which requires much experience and skill for accurate diagnosis. To lower the likelihood of wrong diagnosis, the heart images are shown in 3D view rather than 2D, which is more informative and circumvents the need for highly experienced cardiologists. However, navigating through sequential poses of a deformation in 3D might be inconvenient for human. This urges a deformation anal-

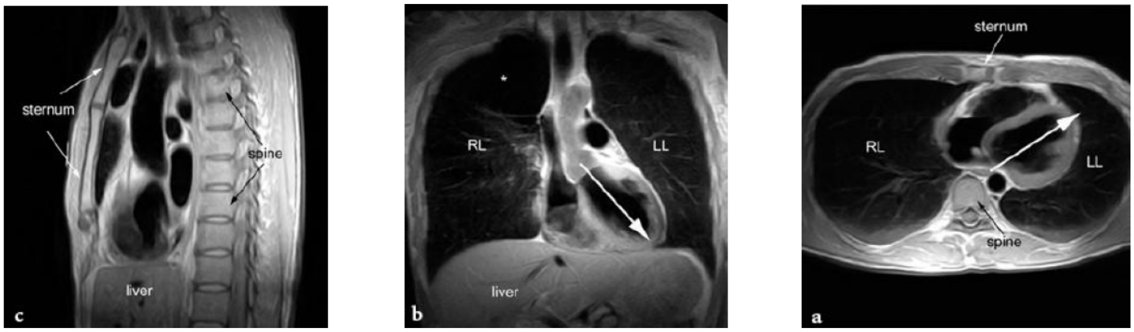

Figure 3.17: The cardiac MRI.

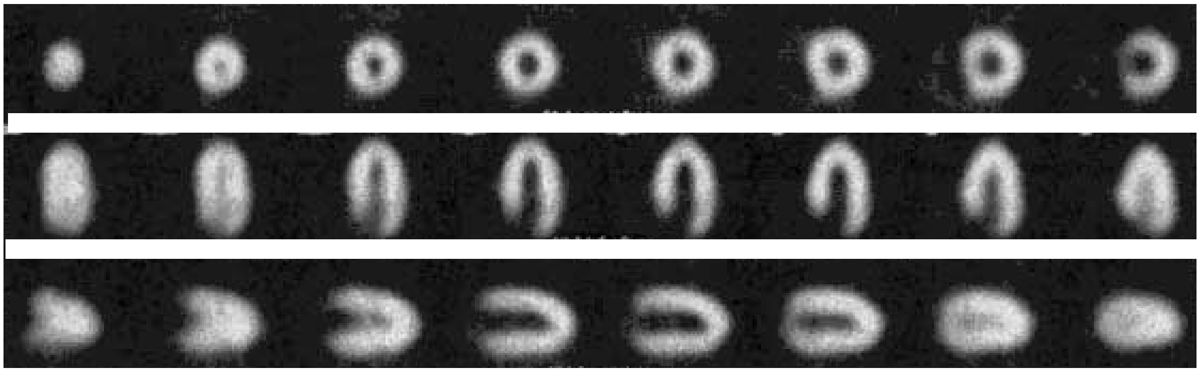
(a)

Figure 3.18: The gated images of the left ventricle at some time points.

ysis method which analyzes and classifies the 3D heart deformations. Our experimental results show that the shape space has the potential to classify the left ventricle deformation.

3.6.1 Data Acquisition and Preparation

A total of 23 gated images of the left ventricle during one heart cycle were acquired from some subjects (9 healthy and 14 patients). Each dataset contains 8 poses of the resolution $128 \times 128 \times 47mm^3$ (Fig. 3.18). To classify the left ventricle deformations, the left ventricle surface should be extracted beforehand (Fig. 3.19). The preprocessing procedure includes the following steps,

- *Blurring the input image*: Due to noise in the gated images, we blur them using some

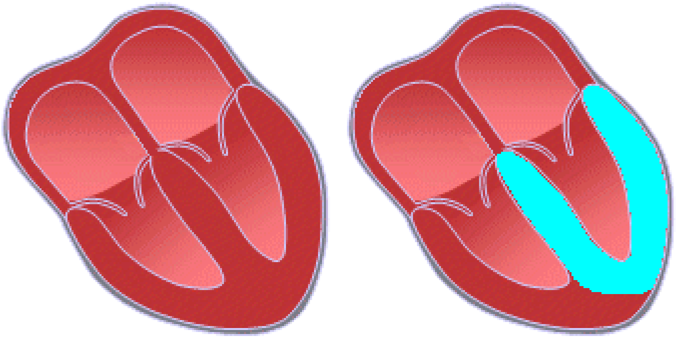
(a) (b)

Figure 3.19: (a) The diagram of the human heart, (b) the left ventricle, labeled in cyan, is extracted from the heart to generate the 3D mesh.

Gausisan filters,

- *Alignment of horizontal and vertical long axis with the z axis*: The blurred 3D image is reoriented to align the horizontal and vertical long axis with the z axis,
- *Surface extraction*: The surface of the high intensity portion of the image is extracted by the Marching Cube algorithm; this portion mostly includes the left ventricle and the liver.
- *Manually editing of the extracted surface*: In the extracted surface, the liver is attached to the left ventricle; therefore, in this step, the liver is removed manually and the surface of the left ventricle is achieved.
- *Surface normalization*: In the last step, the dataset of each deformation is transferred to the origin and normalized to a unit bounding box.

As mentioned, during each heartbeat cycle, 8 sequential cardiac images are acquired. Fig. 3.20 represents 8 meshes, from left to right, corresponding to the LV deformation at sequential time points. Notice that the poses at time points 7 and 3 correspond to the end of diastole and end of systole, respectively.

3.6.2 The Experimental Results of the Quasi-Conformal Shape Space

After extraction of the left ventricles sequential meshes, the intra-subject and inter-subject registrations are performed to find the corresponding points among meshes.

To accomplish this, a total of 16 landmarks are chosen on meshes manually (Fig. 3.21), and then the *constrained thin plate spline* method is used to perform the registration ([106], [23]). As can be seen in Fig. 3.21.a, the area connecting the left ventricle to the right one is cut to make a *boundary*, which is used to set the landmarks.

The left ventricle deformation can be divided into four parts as (*i*) clockwise rotation, (*ii*) contraction (*iii*) expansion, (*iv*) counter clockwise rotation (Fig. 3.22.b). The projected deformation of the left ventricle confirms the previous argument in 2D projection (Fig. 3.23).

Shown by circles in Fig. 3.23, the normal datasets are almost located in the same part of the 2D plane using the classification algorithm.

Fig. 3.24 demonstrates the normal and abnormal deformations in the 3D spatiotemporal space, in which the normal deformations follow the same pattern, which causes their corresponding points in the 2D plane to be close to each other. In fact, adding the extra temporal dimension is necessary, as it takes into account the speed of the deformation which is of utmost importance in heart diagnosis.

3.7 Summary

An algorithm is presented to classify and compare deformations based on a novel quasi-conformal metric in shape space. To make deformation paths intuitively comparable in shape space, the deformations are transferred and projected onto a 2D plane, where each point corresponds to one deformation. The results on synthetic datasets verify the performance of the classification framework.

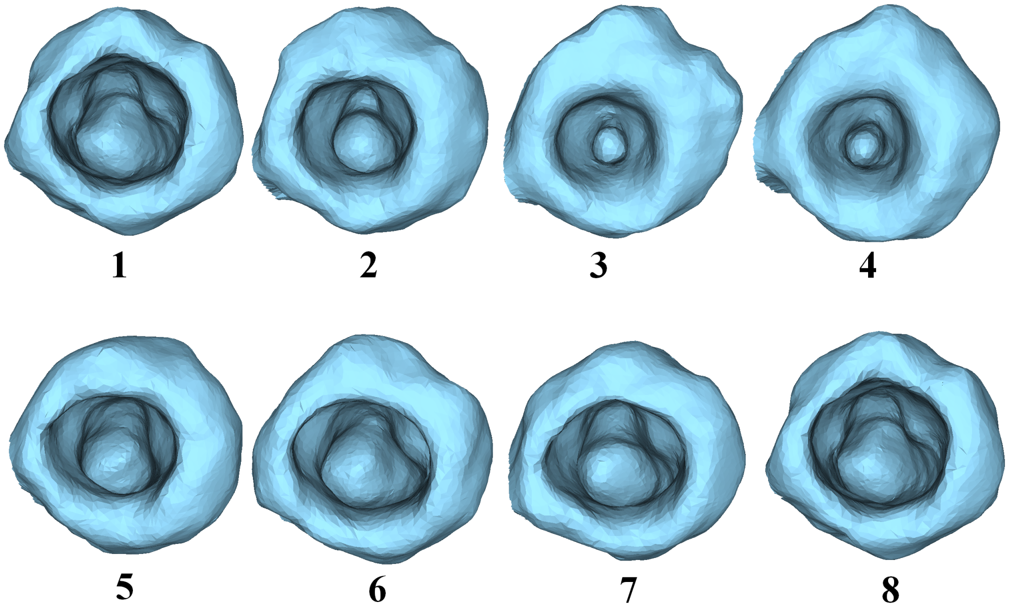

(a)

Figure 3.20: Eight poses, from left to right, corresponding to the LV deformation during one heart cycle.

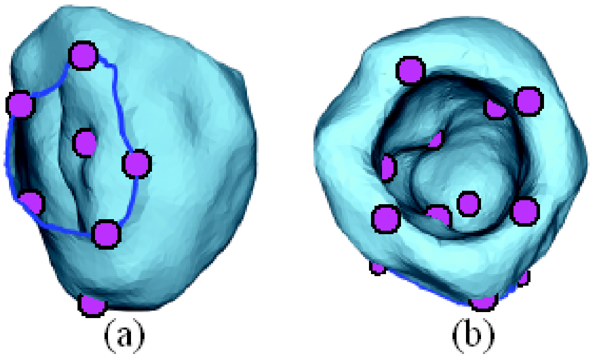
(a) (b)

Figure 3.21: The landmarks are chosen, a) on the boundary, b) inside the ventricle.

Note that if the temporal resolution of the poses is acceptable, the interpolation step can be skipped, thus the rest of the pipeline is executed in $O(n^2)$ time. Otherwise, to increase the temporal resolution a nonlinear function should be optimized, whose complexity is $O(mn)$, where n is the number of meshes, each having m vertices. Thus, the total time complexity of the pipeline is $O(mn) + O(n^2)$. Since each point of shape space corresponds to one mesh in $\mathbb{R}^3$, we can easily retrieve the intermediate meshes [99]. To speed up the algorithm, we employ the space refinement, in which the spatial resolution of meshes is increased iteratively,

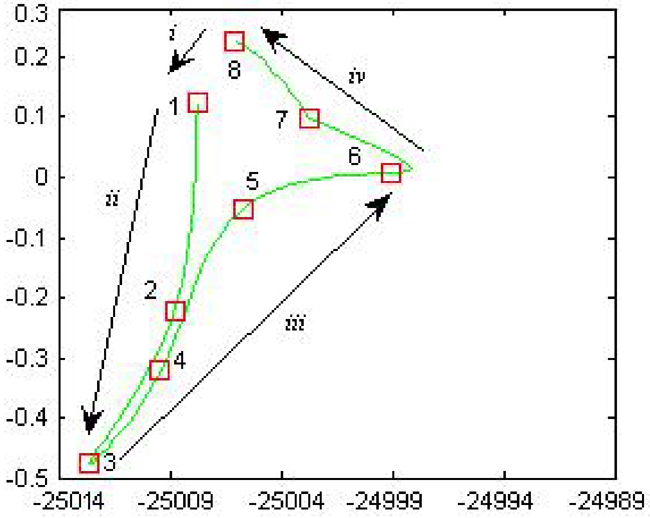

(a)

Figure 3.22: The 2D spatial shape space shows the deformation path of the heart deformation along with the projections of 8 sequential poses onto the spatial shape space (red squares).

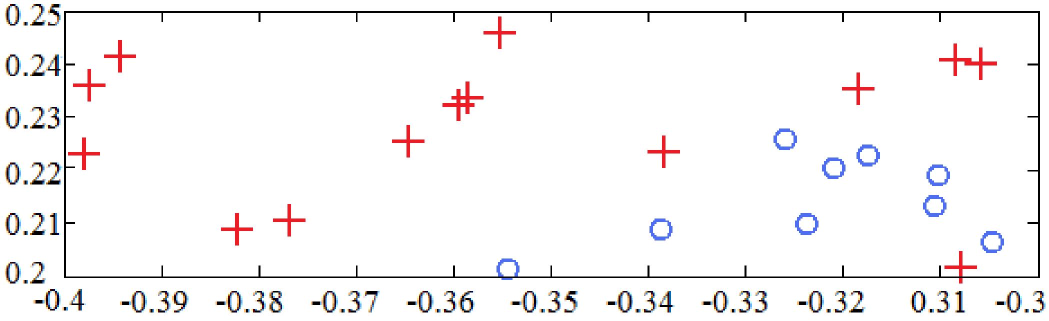

Figure 3.23: The classification of normal (circles) and abnormal (crosses) subjects, in which the two axes are the first two coordinates of LLE.

from coarser meshes to finer ones to get the intermediate poses. As in the methods based on the functional energy minimization ([58], [44]), this method cannot guarantee that no self intersection would occur during interpolation.

Cardiologists usually interpret electrocardiogram signals or use 2D images of the heart for diagnosis, which requires high skill and experience and increases the chance of wrong diagnosis. In contrast, representing the heart in 3D eases the accurate diagnosis procedure, which in turn, requires a 3D deformation analysis method.

We applied our quasi-conformal shape space on the left ventricle deformation of some healthy and patient subjects. The experimental results show the effectiveness of this classi-

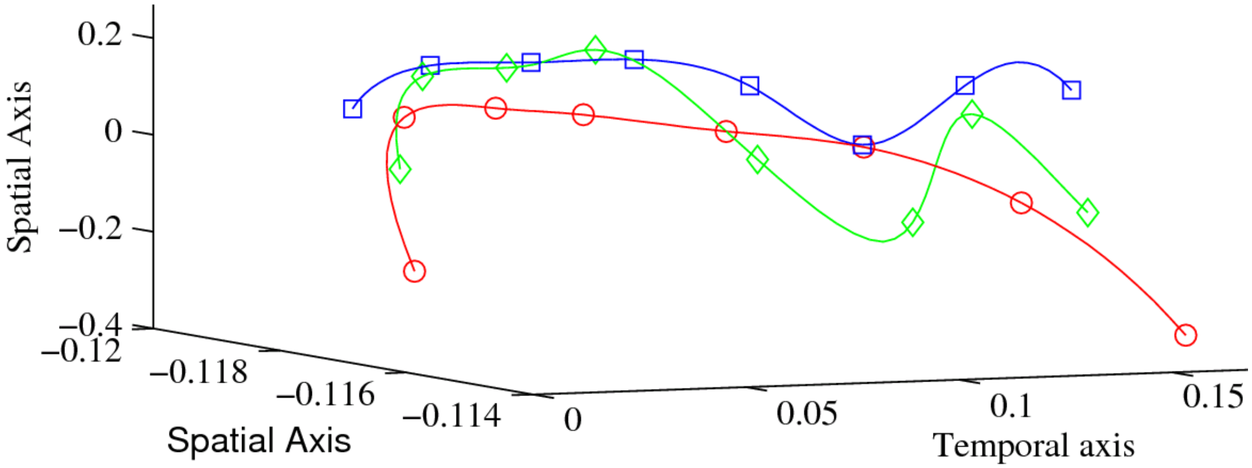

Figure 3.24: Two normal subjects (*squares and diamonds*), and one abnormal subject (*circles*) in the 3D spatiotemporal space.

fication framework to differentiate normal and abnormal subjects based on the geometrical information. Furthermore, the proposed method shows acceptable resistance against different noises. This makes the method a powerful tool, as we use the gated images which might contain either Poisson or Gaussian noise depending on the number of channels used during the image acquisition.

However, automatic localization of the abnormality on the left ventricle is of great importance in the diagnosis procedure. In the next chapter, a new classification framework based on the medial surface and thickness function is introduced which can spot the abnormality on the left ventricle.

CHAPTER 4

THE MEDIAL SURFACE SHAPE SPACE

The wall thickness is known as a valuable measure for the cardiac diagnosis. From the geometrical point of view, it can be considered as a function on the 2D manifold of the medial axis. Therefore, one can diagnose the heart by analyzing this non-linear manifold. This chapter presents a novel classification method based on the shape space of the medial axis to diagnose and spot the abnormality of the left ventricle.

4.1 Introduction

Non-linear shape models yield more accurate model and variations of the shape compared with linear shape models which are combinations of local translations. The medial surface model is a valuable framework to describe shape parameters such as local thickness and bending which do not belong to the Euclidean space. As these parameters belong to the Riemannian symmetric space, linear shape analysis techniques do not apply to them. As aforementioned, Kendall formulates shape spaces as complex projective spaces [56]. Shapes are constructed as infinite-dimensional manifolds and their variations as the diffeomorphism action group ([32], [68]). Some metrics are introduced on the space of planar curves ([69], [83]).

The medial locus is a means of representing the skeleton of a geometric object, which plays an important role in the human perception [12]. The medial locus of a 3D object consists of the centers of all spheres that are interior to the object and tangent to the object's boundary at two or more points. In fact, medial representation, m-rep, incorporates a rich mathematical theory [21], which has many applications in the shape analysis and image processing [76].

Yushkevich et al introduce the parametric representation of the boundary-medial relationship as two continuous parametric manifolds, which provide the ground to fit shape-based coordinate systems to the interiors of objects [103]. Terriberry et al present a 3D medial surface based on subdivision surfaces, which is parameterized over a fixed domain and can support the complex medial surface with more than one medial surface [93]. Sun et al applied the medial model to the right and left ventricle datasets of some subjects and concluded that the medial model can capture the deformation of the left and right ventricles along with the changes of their wall thickness over time ([89], [88]).

Our contributions in this chapter can be summarized as follows,

- A novel shape space based on the medial surface and thickness function is introduced,
- Two shape descriptors are introduced which discriminate different deformations and spot their differences,
- The effectiveness of the medial surface shape space is investigated for classification of the left ventricle deformation.
- The proposed shape space can spot the abnormality on the left ventricle as well.

In this section, some global/local geometrical and physical measures of the cardiac diagnosis are described briefly.

4.1.1 Global Cardiac Volumetric Measures

Use of geometric models is not completely new to the analysis of cardiac images. The traditional methods of obtaining parameters were based on geometrical models as follows,

- Left Ventricular Volume (*LVV*): To estimate the volume of the left ventricle, the LV volume is modeled as the volume of a single shape (e.g., truncated ellipse), or as the sum of multiple smaller volumes of similar configuration, or as a combination of different figures [97].
- Left Ventricular Mass (*LVM*): *LVM* is mainly determined by two factors: chamber vol-

ume, and wall thickness. *LVM* is defined as,

$$V_m = V_t^{epi} - V_c^{endo},$$

$$LVM = d_m \cdot V_m,$$

where $d_m = 1.05g/cm$ is the density of the muscle tissue, V_m is the myocardium volume, V_t^{epi} is the total volume contained within the epicardial borders of the ventricle, and V_c^{endo} is the chamber volume.

- Stroke Volume (*SV*): *SV* is the volume ejected between the end of diastole and the end of systole,

  $$SV = EDV - ESV,$$

  where EDV is the end of diastolic volume, and ESV is the end of systolic volume.

- Ejection Fraction (*EF*): *EF* is a global measure of LV fiber shortening and the LV pump function, which defined as,

  $$EF = \frac{SV}{EDV} \cdot 100\% = \frac{EDV - ESV}{EDV} \cdot 100\%.$$

- Cardiac Output (*CO*): The quantity of oxygenated blood flow, called the Cardiac Output (*CO*), is expressed as,

  $$CO = SV \times HeartRate.$$

  In patients with mitral or aortic regurgitation, or with extensive wall motion abnormalities, the computed *CO* with angiocardiography is erroneous. The 3D imaging techniques provide a potential solution to this problem.

4.1.2 Local Cardiac Shape Descriptors

Three-dimensional model-based analysis of LV shape and motion has the potential of providing rich morphological and functional information. Current clinical assessment of cardiac function is based mainly on global parameters as *LVV* and *EF*. However, some local shape descriptors provide valuable information for the shape analysis.

- Strain Analysis (*SA*): The Strain Analysis is a method to describe the internal deformation of a continuum body. The *reference state* is an initial configuration with respect to which the position of any point is measured to describe the deformation of a body.

  Assume two neighboring myocardial points, $\{y_i\}$, $\{y_i + \Delta y_i\}$, move to $\{x_i\}$, $\{x_i + \Delta x_i\}$, respectively. Also, $x_i = y_i + u_i$, where u_i is the displacement. By taking the deformation gradient, one can calculate the changes in length between the two neighboring points before and after the deformation, that's, dL_y and dL_x. Then,

  $$dL_x^2 - dL_y^2 = 2\sum_{i=1}^{3}\sum_{j=1}^{3} E_{ij}\,dy_i dy_j,$$

  Where E is the *strain tensor*,

  $$E_{ij} = \frac{1}{2}\left(\frac{\partial u_i}{\partial y_j} + \frac{\partial u_j}{\partial y_i} - \sum_{k=1}^{3}\frac{\partial u_k}{\partial y_j}\cdot\frac{\partial u_k}{\partial y_i}\right).$$

- Mean and Gaussian Curvature: By analyzing Gaussian curvature ($K = k_1 \cdot k_2$) and the mean curvature ($H = (k_1 + k_2)/2$), one can locally distinguish between different surface types, where k_1 and k_2 are the principal curvatures measure the maximum and minimum bending of a regular surface. The distribution of the Gaussian curvature in the LV at different phases of the cardiac cycle is structurally stable over time [27].

  Whereas the LV free wall provides rich and dense curvature information, the curvature at the septal wall is less suitable to establish point correspondences. Similar findings were made by Sacks *et al.* [81] with respect to the RV free wall: the RV free wall has relatively uniform distribution of principal curvatures, and the surface geometry of the RV free wall does not change significantly from end diastole to end systole.

- Shape Index and Shape Spectrum: Although mean and Gaussian curvatures are related to the concept of curvedness, there still remains scale information in these shape descriptors. To overcome this problem, Clarysse *et al.* [18] have used the shape index (s) and the curvedness (c),

  $$s = \frac{2}{\pi} \cdot \arctan\left(\frac{k_1 + k_2}{k_1 - k_2}\right),$$

  $$c = \left(\frac{k_1^2 + k_2^2}{2}\right).$$

  While c is inversely proportional to the object size, s defines a continuous distribution of surface types ranging from cup-like umbilic (s = -1) to peak-like umbilic points (s = +1). It is shown that s is invariant to orientation preserving similarity transformation, yet c is not.

  In [75], the shape spectrum is introduced as a global shape index,

  $$\gamma(h,t) = \frac{1}{A} \int\int_S \delta\left(s\left(x\right) - h\right).ds,$$

  where

  $A = \int\int_S ds$: The total area of the surface S, ds: An small region around the point x, $\delta\left(\cdot\right)$: The Dirac delta function.

- Local stretching: A conformal motion can be described as a spatially-variant but locally isotropic stretching factor. The *local stretching factor* τ is computed from the change in

Gaussian curvature and a polynomial stretching model as,

$$\bar{K} = \frac{K}{\tau^2} + \frac{f\left(E, F, G, \tau, \tau_u, \tau_v, \tau_{uu}, \tau_{vv}\right)}{\tau^2},$$

where

$f\left(\cdot\right)$: A linear or quadratic polynomial stretching model,

E, *F*, *G:* coefficients of the first fundamental form,

(u, v): coordinates of a local parameterization of the surface patch.

The local epicardial stretching factors computed over the cardiac cycle follow a similar evolution to the temporal variation of the principal strains obtained using *SA* techniques.

- Wall Thickening (WT): Wall Thickening is studied in the detection of dysfunctional myocardium, and is a sensitive indicator of dysfunctional contraction [3]. In some researches, the local wall thickness (*LWT*) is defined as,

$$LWT = \frac{V_c}{A},$$

where

V_c: The volume of the small cuboids element of the myocardium,

A: The average area of its endocardial and epicardial surfaces.

In many researches, the WT is computed from the *centerline* method [84]. Starting with the endocardial and epicardial contours at each slice, the centerline method measures WT in chords drawn perpendicular to a line that is equidistant to both contours (the centerline) (Fig. 4.1). As a 3D extension of the centerline method, the *medial surface* method makes use of a reference medial surface to compute the chords and subsequent wall thickness [13].

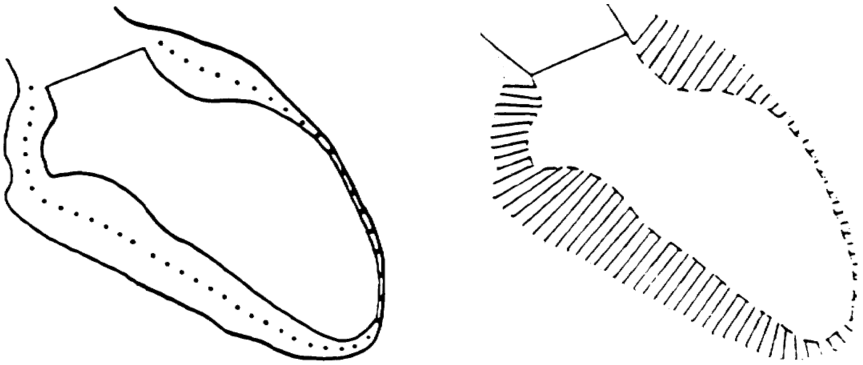

Figure 4.1: The WT is computed from the centerline method at each slice.

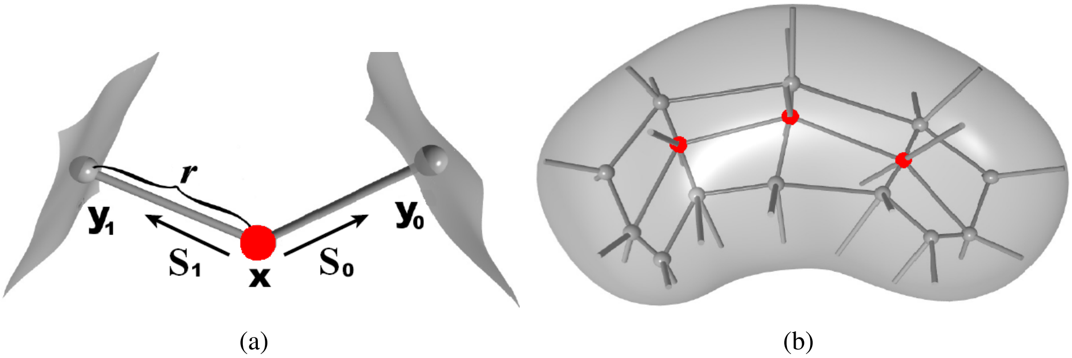

(a)

(b)

Figure 4.2: (a) An atom has a position ($\mathbf{x}$), radius (r), and two spoke directions ($\mathbf{S}_0$, $\mathbf{S}_1$), (b) The regular atoms are non-boundary atoms of the medial surface (Red atoms).

4.2 The Medial Surface

In the m-reps framework, the *medial surface* consists the centers of the inscribed spheres and two or three vectors, called spokes, from the sphere centers to the two or three tangent points on the object boundary. Indeed, the medial surface is a topological disk with a smooth edge, which is constituted by the medial locus.

An *atom* contains a position ($\mathbf{x}$), radius (r), two spokes ($\mathbf{S}_0$, $\mathbf{S}_1$) (Fig. 4.2). Thus an atom can be represented by $(\mathbf{x}, r, \mathbf{S}_0, \mathbf{S}_1) \in \mathbb{R}^3 \times \mathbb{R}^+ \times S^2 \times S^2$, and its corresponding boundary points $\mathbf{y}_0$, $\mathbf{y}_1$ can be achieved as, $\mathbf{y}_0 = \mathbf{x} + r\mathbf{S}_0$, $\mathbf{y}_1 = \mathbf{x} + r\mathbf{S}_1$, where $\mathbf{S}_0$, $\mathbf{S}_1$ are of lengths $r\mathbf{S}_0$, $r\mathbf{S}_1$, respectively.

An *end atom* is a kind of atom that is located on the boundary of the medial surface, and has an extra spoke in the bisector direction, $\mathbf{b}$, whose length is ηr, where η is in $[1\ 1/\cos(\theta)]$

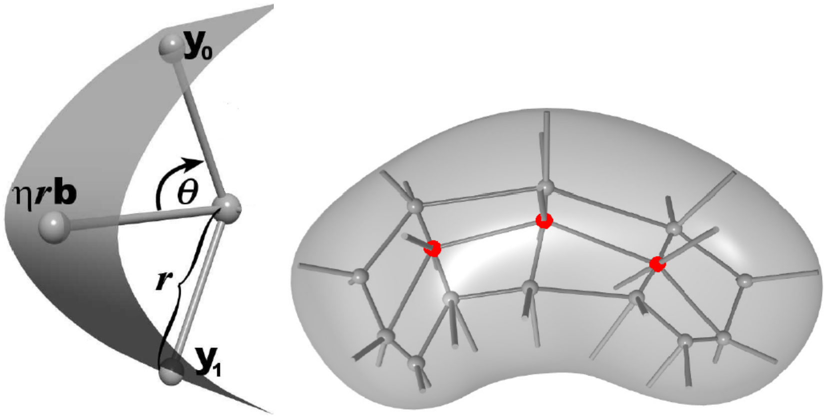

(a) (b)

Figure 4.3: (a) An end atom has a position ($\mathbf{x}$), radius (r), and three spoke directions ($\mathbf{S}_0$, $\mathbf{S}_1$, $\eta r\mathbf{b}$), (b) The end atoms are on the boundary of the medial surface (Gray atoms).

(Fig. 4.3). If $\eta = 1/\cos(\theta)$, the boundary is sharp, and if $\eta = 1$, the boundary is circular. The atoms can be thought as control points on a continuous medial surface. Indeed, the continuous medial surface are extended beyond the end atoms to the boundary of the object, where the boundary of the continuous medial surface is achieved by $\mathbf{y}_0$, $\mathbf{y}_1$ and their corresponding normal vectors $\mathbf{S}_0$, $\mathbf{S}_1$ [95]. A medial structure needs to hold some conditions to imply a legal boundary without any singularity [21].

4.3 The Exponential Map

A group action is a transformation of the manifold **M**, just as matrices are transformations of the Euclidean space. A *Lie group* **G** is a differentiable manifold which describes the transformations of smooth manifolds, and forms an algebraic group (the tangent space to the identity element of **G**) such that both *Inverse* and *Multiplication* operations are differentiable mappings as well [61],

$$Multiplication : (x, y) \in \mathbf{G} \times \mathbf{G} \to xy \in \mathbf{G},$$

$$Inverse : x \in \mathbf{G} \to x^{-1} \in \mathbf{G}.$$

For instance, rotations, translations, and affine transformations in $\mathbb{R}^n$ are some Lie groups.

In fact, the Lie group actions are used to compute the geodesic on the Riemannian symmetric spaces such as Euclidean space, $\mathbb{R}^n$, spheres, S^n, and hyperbolic space, $\mathbb{H}^n$.

Definition: The *isotropy* subgroup of the base point $\mathbf{b} \in \mathbf{M}$ is the subgroup of $\mathbf{G}$ which leaves $\mathbf{b}$ fixed, that's, $\mathbf{G_b} = \{g \in \mathbf{G} : g \cdot \mathbf{b} = \mathbf{b}\}$.

Theorem 1: Let $\mathbf{M}$ be a symmetric space and let the isometry group $\mathbf{G}$ act transitively on $\mathbf{M}$. Then the map,

$$\varphi : \mathbf{G}/\mathbf{G}_b \to \mathbf{M},$$

is a diffeomorphism [86].

Corollary 1: Every symmetric space $\mathbf{M}$ is geodesically complete, i.e., any two points in the same path component of $\mathbf{M}$ can be connected by a geodesic [52].

Let $\mathbf{M}$ be a complete Riemannian manifold, which implies there exists a geodesic between each pair of points on $\mathbf{M}$. Let $v \in T_x\mathbf{M}$ be a tangent vector, thus there exists a unique geodesic $\gamma_v(t)$, where $\gamma_v(0) = x$ and $\gamma_v'(0) = v$. The *exponential map* $Exp_x(v) : T_x\mathbf{M} \to \gamma_v(t)$ maps the vector v to a point on the geodesic $\gamma_v(t)$. The exponential map preserves the distance from the initial point x, that's, $d(x, Exp_x(v)) = \|v\|$, thus it is a diffeomorphism in a neighborhood of zero. Its inverse on the Riemannian manifold is called Log map, Log_x. Let $x, y \in \mathbf{M}$ be two points in a neighborhood on $\mathbf{M}$, then the geodesic between x and y is $d(x, y) = \|Log_x(y)\|$.

4.3.1 The Exponential map on S^2

For the sphere S^2 with the base of $\mathbf{p} = (0, 0, 1)$, the Exponential map on S^2 is,

$$Exp_{\mathbf{p}}(v) = \left(v_1 \cdot \frac{\sin\|v\|}{\|v\|}, v_2 \cdot \frac{\sin\|v\|}{\|v\|}, \cos\|v\|\right), \tag{4.1}$$

where $v = (v_1, v_2, 0) \in T_{\mathbf{p}}S^2$ is a tangent vector in the plane x-y (Fig. 4.4). Inversely, the Log map the point $\mathbf{x} = (x_1, x_2, x_3) \in S^2$ on the tangent plane $T_{\mathbf{p}}S^2$ is,

$$Log_{\mathbf{p}}(x) = \left(x_1 \cdot \frac{\theta}{\sin(\theta)}, x_2 \cdot \frac{\theta}{\sin(\theta)}\right), \tag{4.2}$$

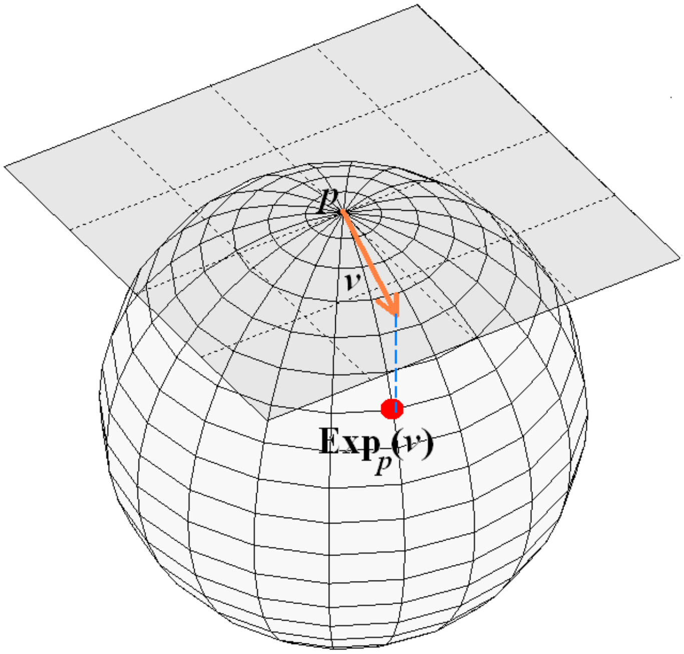

Figure 4.4: The exponential map of the tangent vector v on the sphere S^2.

where $\theta = \arccos(x_3)$ is the spherical distance between the point **p** and **x**. Indeed, S^2 is a symmetric space, which can be written as $S^2 = SO(3)/SO(2)$, where $SO(2)$ is the isotropy subgroup of **p** which contains all rotations about the z axis. According to Corollary 1, S^2 is a complete space; therefore, every two points can be connected to each other by a geodesic, which is the great circle passing through **p**.

4.3.2 The geodesic distance between the medial surfaces

Let $\mathbf{M} = \{\mathbb{R}^3 \times \mathbb{R}^+ \times S^2 \times S^2\}$ be the symmetric space of the medial atoms, and the Lie group $\mathbf{G} = \{\mathbb{R}^3 \times \mathbb{R}^+ \times SO(3) \times SO(3)\}$ act on it smoothly as,

$$\mathbf{G} \times \mathbf{M} \to \mathbf{M} : g \cdot \mathbf{m} = (\mathbf{v}, s, \mathbf{R}_0, \mathbf{R}_1) \cdot (\mathbf{x}, r, \mathbf{S}_0, \mathbf{S}_1) = (\mathbf{x} + \mathbf{v}, r \cdot s, \mathbf{R}_0 \cdot \mathbf{S}_0, \mathbf{R}_1 \cdot \mathbf{S}_1)\,.$$

If the base atom $\mathbf{b} \in \mathbf{M}$ is $\{(0,0,0), (1), (0,0,1), (0,0,1)\}$, the isotropy subgroup $\mathbf{G_b}$ is,

$$\{(0,0,0) \times (1) \times SO(2) \times SO(2)\}\,.$$

According to Theorem 1, the medial surface is diffeomorphic the quotient space,

$$\mathbf{G}/\mathbf{G_b} = \left\{\mathbb{R}^3 \times \mathbb{R}^+ \times SO(3)/SO(2) \times SO(3)/SO(2)\right\}.$$

Let $\mathbf{p} = [(0,0,0),(1),p_0,p_1] \in \{\mathbb{R}^3 \times \mathbb{R}^+ \times S^2 \times S^2\}$ be the base point, p_0 = p_1 = (0, 0, 1), and $\mathbf{u} = [\mathbf{x}, r, \mathbf{v}_0, \mathbf{v}_1]$ be the tangent vector of **M**, where $\mathbf{v}_0$ and $\mathbf{v}_1$ are the spherical tangent vectors. Therefore, the exponential of the medial surface is,

$$Exp_p(\mathbf{u}) = \left\{\mathbf{x}, e^r, Exp_{\mathbf{p}_0}(\mathbf{v}_0), Exp_{\mathbf{p}_1}(\mathbf{v}_1)\right\},$$

where $Exp_{\mathbf{p}_0}(\mathbf{v}_0)$, $Exp_{\mathbf{p}_1}(\mathbf{v}_1)$ are the two spherical exponential maps defined in Eq.4.1. The corresponding Log map of $\mathbf{m} = (\mathbf{x}, r, \mathbf{S}_0, \mathbf{S}_1) \in \mathbf{M}$ is,

$$Log_p(\mathbf{m}) = \left\{\mathbf{x}, \log(r), Log_{\mathbf{p}_0}(\mathbf{S}_0), Log_{\mathbf{p}_1}(\mathbf{S}_1)\right\},$$

where $Log_{\mathbf{p}_0}(\mathbf{S}_0)$, $Log_{\mathbf{p}_1}(\mathbf{S}_1)$ are the two spherical log maps defined in Eq.4.2. In general, the distance between two corresponding atoms $\mathbf{m}_1$ and $\mathbf{m}_2$ is,

$$d(\mathbf{m}_1, \mathbf{m}_2) = \left\|Log_{\mathbf{m}_1}(\mathbf{m}_2)\right\|,$$

where the norm of the tangent vector $\mathbf{u} = [\mathbf{x}, r, \mathbf{v}_0, \mathbf{v}_1]$ achieved by the above log map is,

$$\|\mathbf{u}\| = \sqrt{\|\mathbf{x}\|^2 + \rho \cdot \|r\|^2 + \|\mathbf{v}_1\|^2 + \|\mathbf{v}_2\|^2},$$

where ρ is the average radius over all corresponding atoms. Accordingly, the geodesic distance between two medial surfaces $\mathbf{M}_1$ and $\mathbf{M}_2$ each having *n* atoms is,

$$d(\mathbf{M}_1, \mathbf{M}_2) = \sum_{i=1}^{n} d(\mathbf{m}_i, \acute{\mathbf{m}}_i), \tag{4.3}$$

where $\mathbf{m}_i \in \mathbf{M}_1$ and $\acute{\mathbf{m}}_i \in \mathbf{M}_2$.

4.4 The Left Ventricle Shape Descriptor

This study aims to classify the normal and abnormal left ventricle (LV) deformations based on the changes in the Wall Thickening (WT) of LV. *Cardiomyopathy* is the main cardiac disease which affects the wall thickness and its functionality. There are three types of Cardiomyopathy (Fig. 4.5):

- *Dilated cardiomyopathy* (DCM): A portion of the myocardium is dilated, often without any obvious cause. In this condition, the heart becomes weakened and enlarged and cannot pump blood efficiently [46].
- *Hypertrophic cardiomyopathy* (HCM): a portion of the myocardium thickened without any obvious cause [78].
- *Restrictive cardiomyopathy* (RCM): The walls are rigid, and the heart is restricted from stretching and filling with blood properly [1].

In many researches, the WT is computed from the centerline method. Here, in this study the medial surface is computed, and its features are extracted during one heart cycle for each

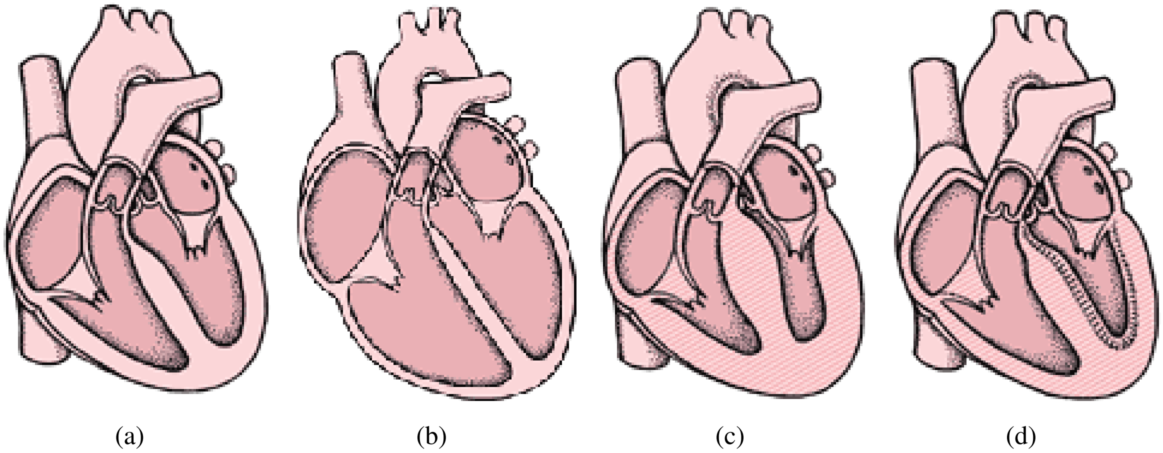

(a) (b) (c) (d)

Figure 4.5: The diagram of a normal heart, (b) The heart with Dilated cardiomyopathy, (c) The heart with Hypertrophic cardiomyopathy, (d) The heart with Restrictive cardiomyopathy.

Table 4.1: The changes of the left ventricle wall thickness over time for healthy hearts and hearts with cardiomyopathy

	t_1 and t_2 are in Contraction phase ($t_1 < t_2$)	t_1 and t_2 are in Expansion phase ($t_1 < t_2$)
Healthy heart	$1 < r(t_2)/r(t_1)$	$r(t_2)/r(t_1) < 1$
Portions with cardiomyopathy	$r(t_2)/r(t_1) \approx 1$	$r(t_2)/r(t_1) \approx 1$

kind of cardiomyopathy.

Let $\mathbf{M}(t)$ be the medial surface at time t, and $\mathbf{m}(t) = \{\mathbf{x}(t), r(t), \mathbf{S}_0(t), \mathbf{S}_1(t)\} \in \mathbf{M}(t)$ be an atom of $\mathbf{M}$ at time t. If the heart cycle is divided into two phases of contraction and expansion, the changes of WT over time for a heart with cardiomyopathy and a healthy heart are illustrated in Table 4.1.

In fact, the portion of the heart with cardiomyopathy cannot contract or expand as a healthy heart, thus the proportion of the thickness (*PT*), $r(t_2)/r(t_1)$, is roughly equal to one (Table 4.1).

It seems *PT* yields a good measure to spot the abnormalities on LV. However, due to existence of noise and trend in the acquired images, and also lack of accuracy in the extracted medial surface, *PT* values of some atoms in the healthy subjects might be close to one as well. This lowers the accuracy of *PT* as a reliable measure. To tackle this problem, two measures are introduced which can confirm the accuracy of the *PT* values.

4.4.1 Average of the Normal Vectors (ANV)

Let $\hat{\mathbf{M}}$ be the set of all atoms whose *PT* values are around one. According to our experiments, the portion of LV with cardiomyopathy looks like a patch (Fig. 4.6), and the direction of the average of the normal vectors (ANV) in $\hat{\mathbf{M}}$ does not change so much over time.

Fig. 4.6.a illustrates the deformation of LV with an abnormality shown as a patch along with its normal vectors. As mentioned, the portion of the LV having cardiomyopathy has *PT* values roughly equal to one; the direction of ANV does not change considerably at sequential time points, which is represented in Fig. 4.6.b.

In contrast, in the healthy LV's, there might be some atoms whose *PT* values are close to

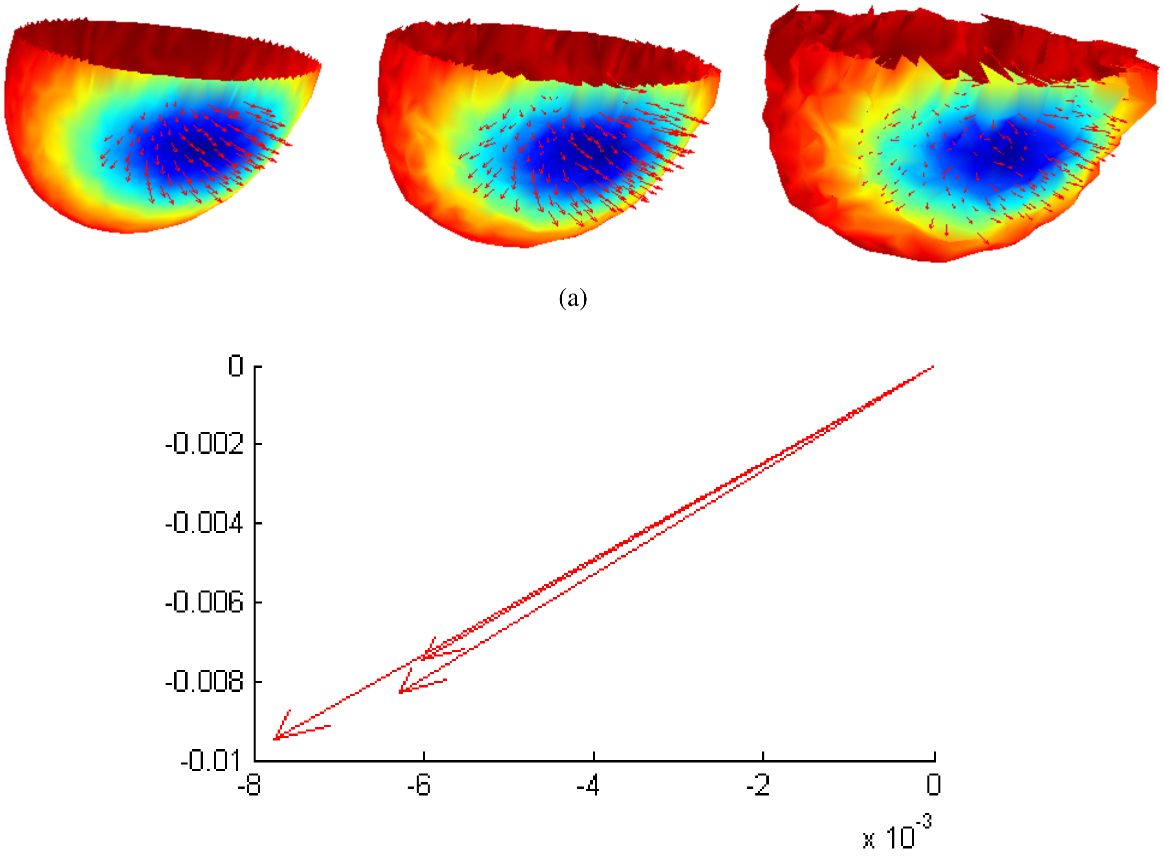
(a)

(b)

Figure 4.6: (a) The medial axis of the LV at three time points from left to right along with the normal vectors of atoms in $\hat{\mathbf{M}}$, different colors show different *PT* values. (b) The average of the normal vectors (ANV) of the atoms in $\hat{\mathbf{M}}$ have roughly the same direction.

one. Nevertheless, as there is no abnormality patch as in the abnormal case, the atoms in $\hat{\mathbf{M}}$ change at different time points from one pose to another (Fig. 4.7.a), which results in ANV of the atoms in $\hat{\mathbf{M}}$ being in different directions (Fig. 4.7.b).

4.4.2 Mean of the Positions (MP)

Another measure to confirm the accuracy of *PT* values is the changes of the positions of atoms belonging to the portion with the cardiomyopathy. Let $\mathbf{x}$ be the position of the atom in $\hat{\mathbf{M}}$. Since abnormality looks like a patch, the Mean of the Positions (MP) of atoms in $\hat{\mathbf{M}}$ is close to the medial surface (Fig. 4.8.a), in contrast to the normal LV's in which MP is not close to the medial surface, since the atoms in $\hat{\mathbf{M}}$ are distributed all over the surface and there is no patch

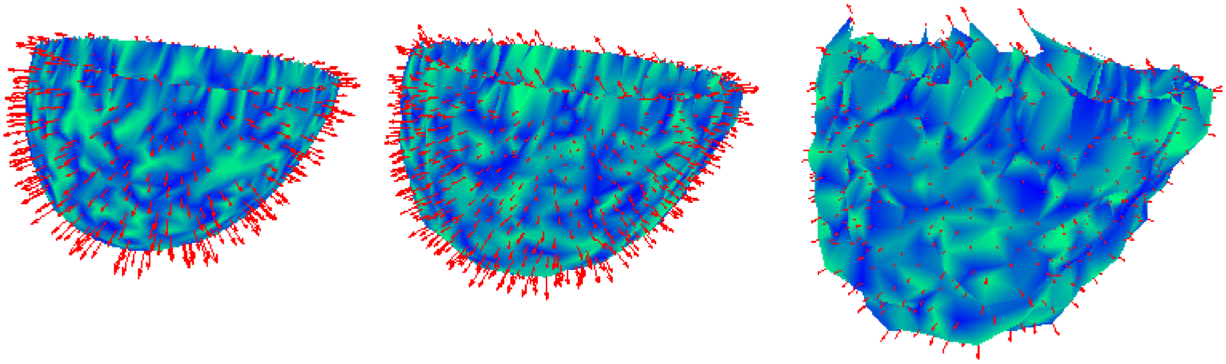
(a)

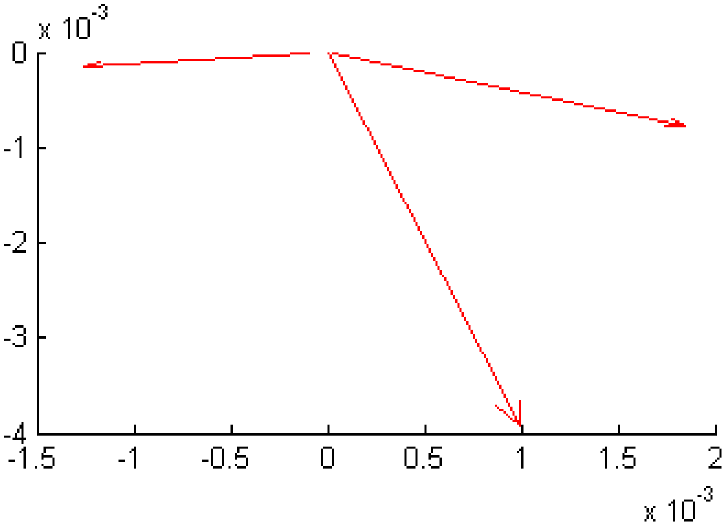

(b)

Figure 4.7: (a) The medial axis of the normal LV at three time points from left to right along with the normal vectors of atoms in $\hat{\mathbf{M}}$, different colors show different *PT* values. (b) ANV of the atoms in $\hat{\mathbf{M}}$ have considerably different directions.

(Fig. 4.8.b). In addition, the variance of the positions of atoms in $\hat{\mathbf{M}}$ is a good differentiating measure. Nonetheless, out experiments show that MP can yield satisfactory results, thus in this study we do not use the variance of the positions.

4.5 Construction of Shape Space

Based on the proposed shape descriptors, a new shape space is constructed in which each point corresponds to one pose rather than one atom. Let **M** be the shape space manifold and

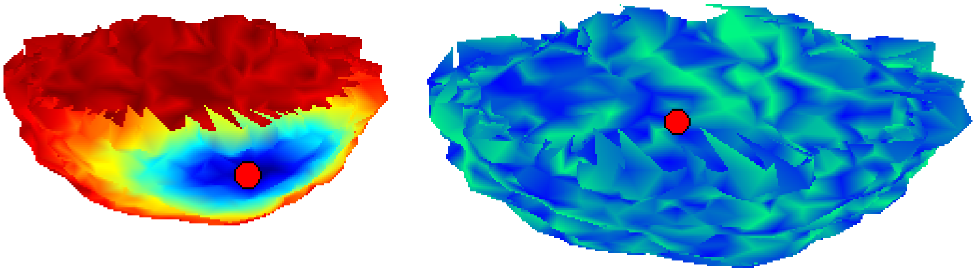

(a) (b)

Figure 4.8: (a) In a LV with cardiomyopathy, the mean of position (MP) of atoms in $\hat{\mathbf{M}}$, shown by a red solid dot, is roughly on the medial surface, (b) In a healthy LV, the mean is inside the medial surface.

$m \in \mathbf{M}$ be a point corresponding to one pose. The new shape space is,

$$\mathbf{m} = (\bar{\mathbf{x}}, \hat{r}^{\rho}, \mathbf{N}^{avg}) \in \left\{\mathbb{R}^3 \times \mathbb{R}^+ \times S^2\right\},$$

where $\bar{\mathbf{x}}$ and $\mathbf{N}^{avg}$ are the MP and ANV of atoms in $\hat{\mathbf{M}}$, and

$$\hat{r} = \prod_{\hat{\mathbf{M}}} \left(\frac{r_{i+1}}{r_i}\right),$$

is the multiplication of *PT* values over all atoms in $\hat{\mathbf{M}}$.

The introduced shape descriptor uses the normal vectors of the medial surface to confirm the accuracy of *PT* values in different subjects. However, the medial surface as mentioned before contains two spokes which are the normal vectors of the boundary, not of the medial surface (Fig. 4.9).

To take this difference into account, the distance between each spoke and the corresponding normal vector is measured by the log map as in Eq.4.2,

$$Log_{\mathbf{N}}(\mathbf{S}) = \left(s_1 \cdot \frac{\theta}{\sin(\theta)}, s_2 \cdot \frac{\theta}{\sin(\theta)}\right),$$

where $\mathbf{N}$ is the normal vector of the medial surface, and $\mathbf{S} = (s_1, s_2, s_3)$ is the spoke. The

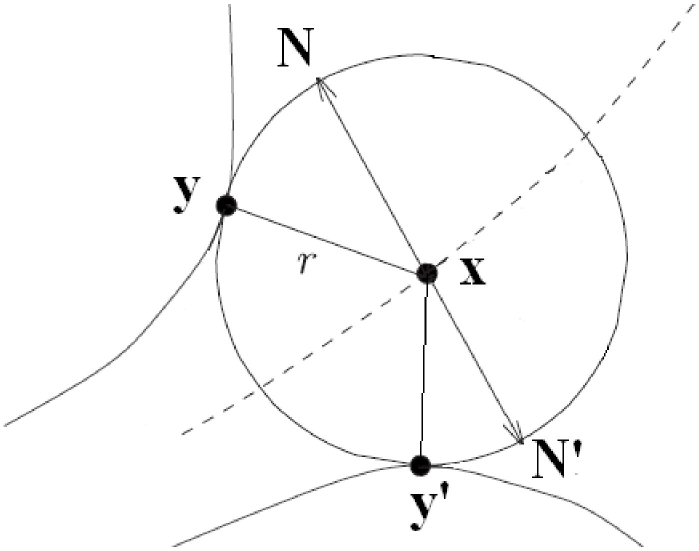

Figure 4.9: The extract medial surface contains two spokes which are perpendicular to the boundary at **y** and **y**′, yet the proposed shape descriptor makes use of the normal vectors, **N** and **N**′, of the medial surface .

average of log map distance between the normal vector **N** and the corresponding spoke **S** over all the atoms in $\hat{\mathbf{M}}$ is,

$$\rho = \frac{\sum_{\hat{\mathbf{M}}} Log_{\mathbf{N}}(\mathbf{S})}{\left|\hat{\mathbf{M}}\right|}.$$

4.5.1 Distance metric

To measure the distance between two points corresponding to two poses in the space **M**, we use the log map distance mentioned before. Let $\mathbf{m}_1 = (\bar{\mathbf{x}}_1, \hat{r}_1^{\rho}, \mathbf{N}_1^{avg})$ and $\mathbf{m}_2 = (\bar{\mathbf{x}}_2, \hat{r}_2^{\rho}, \mathbf{N}_2^{avg})$ be two poses in **M**, and $\mathbf{u}_1$ is the tangent vector of **M** at point $\mathbf{m}_1$. As aforementioned, the geodesic distance between $\mathbf{m}_1$ and $\mathbf{m}_2$ is $d(\mathbf{m}_1, \mathbf{m}_2) = \|Log_{\mathbf{m}_1}(\mathbf{m}_2)\|$. The log map is a distance preserving mapping,

$$\|Log_{\mathbf{m}_1}(\mathbf{m}_2)\| = \|\mathbf{u}_1\| = \langle \mathbf{u}_1, \mathbf{u}_1 \rangle^{\frac{1}{2}}.$$

Let $g = (\mathbf{v}, s, \mathbf{R})$ be an element of **G**, then the group action is,

$$g \cdot \mathbf{m}_1 = (\mathbf{v} + \bar{\mathbf{x}}_1, s \cdot \hat{r}_1^{\rho}, \mathbf{R} \cdot \mathbf{N}_1^{avg}).$$

As in the case of the medial space, the space $\mathbf{M}$ is a quotient space, that's $\mathbf{M} = \mathbf{G}/\mathbf{G}_p$, where $\mathbf{G}$ is a connected group of isometries of M, that's $d(\mathbf{m}_1, \mathbf{m}_2) = d(g \cdot \mathbf{m}_1, g \cdot \mathbf{m}_2)$, and the isotropy subgroup G_p is compact. Let $\mathbf{p} = [(0,0,0),(1),p_0] \in \{\mathbb{R}^3 \times \mathbb{R}^+ \times S^2\}$ be the base point, where $p_0 = (0,0,1)$, and $\bar{g} \in \mathbf{G}$ maps $\mathbf{m}_1$ to $\mathbf{p}$, that's $\mathbf{p} = \bar{g} \cdot \mathbf{m}_1$.

Since $\bar{g}$ is an isometry, $d(\mathbf{m}_1, \mathbf{m}_2) = d(\bar{g} \cdot \mathbf{m}_1, \bar{g} \cdot \mathbf{m}_2) = d(\mathbf{p}, \bar{g} \cdot \mathbf{m}_2)$. It is obvious,

$$\bar{g} \cdot \mathbf{m}_2 = (\bar{\mathbf{x}}_2 - \bar{\mathbf{x}}_1, \frac{\hat{r}_2^{\rho}}{\hat{r}_1^{\rho}}, \mathbf{T} \cdot \mathbf{N}_2^{avg}),$$

where $\mathbf{T}$ is a rotation matrix, such that $\mathbf{T} \cdot \mathbf{N}_1^{avg} = p_0$. On the other hand,

$$Log_{\mathbf{p}}(\bar{g} \cdot \mathbf{m}_2) = (\bar{\mathbf{x}}_2 - \bar{\mathbf{x}}_1, log(\frac{\hat{r}_2^{\rho}}{\hat{r}_1^{\rho}}), Log_{\mathbf{p}}(\mathbf{T} \cdot \mathbf{N}_2^{avg}))$$

As in the medial surface space,

$$d(\mathbf{p}, \bar{g} \cdot \mathbf{m}_2) = \|Log_{\mathbf{p}}(\bar{g} \cdot \mathbf{m}_2)\| = \left(\|\bar{\mathbf{x}}_2 - \bar{\mathbf{x}}_1\|^2 + \|\rho_2 \cdot log(\hat{r}_2) - \rho_1 \cdot log(\hat{r}_1)\|^2 + \|Log_{\mathbf{p}}(\mathbf{T} \cdot \mathbf{N}_2^{avg})\|^2\right)^{\frac{1}{2}},$$

in which, $\|Log_{\mathbf{p}}(\mathbf{T} \cdot \mathbf{N}_2^{avg})\| = \left\|Log_{\mathbf{N}_1^{avg}}(\mathbf{N}_2^{avg})\right\|$. Obviously, the intermediate poses of an abnormal LV are closer to each other using this metric than those of the normal LV.

4.6 Results on Synthetic Data

Some synthetic datasets are produced to assess the performance of the proposed shape space. In the synthetic datasets, we assume that the extracted medial surfaces are 2D connected surfaces and the thickness is a function on the surfaces. Then the 2D mesh is deformed in accordance with a deformation pattern. The thickness function is also changed to simulate the changes of wall thickness in LV. Fig. 4.10 illustrates a synthetic dataset which is similar to the medial surface of LV during the expansion period. Therefore, the medial surface registration

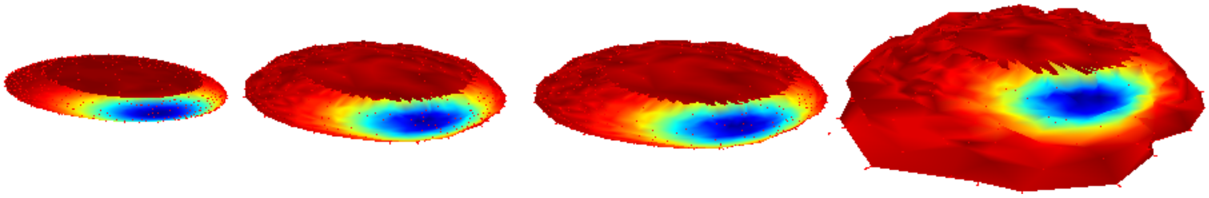

Figure 4.10: The medial surface is simulated by a 2D mesh and the thickness as a function on the 2D surface.

can be circumvented, as the point correspondence is known beforehand.

As aforementioned, the end atoms are the ones on the boundary of the medial surface having an additional spoke. Generally, the end atoms can unstable the image analysis task [61]. To avoid such instability, the end atoms are ignored and only the regular atoms are being used for the analysis purposes.

Some genus zero surfaces with one boundary are deformed in accordance with the LV deformation and different thickness functions are added as a function on the deforming surfaces. After finding the locations in the shape space, the deformation paths are determined for each deformation and projected onto a 2D using the MDS as mentioned before. As expected, the poses of the abnormal deformations with a patch, Fig. 4.10, are close to each other on the 2D plane, yet the normal subjects do not follow a specific deformation path.

4.6.1 Noise Resistance

Being noise resistance is a great concern in all medical imaging techniques; therefore, some noises with uniform and Gaussian distributions are added to the datasets. Let $\mathbf{K}$ be the set of all points corresponding to all medial surfaces and $\mathbf{k}_i$ be the set of points classified in the group i^{th}. In addition, let k_i belong to the set $\mathbf{k}_i$, and l_i be its assigned label. As in Eq.3.6, the statistic τ quantifying the performance of the algorithm as follows,

$$\tau = \frac{\sum_i |\{k_i \in \mathbf{k}_i \mid l_i = i\}|}{|\mathbf{K}|} \,. \tag{4.4}$$

Table 4.2 represents the algorithm performance against additive noises with different dis-

Table 4.2: Performance of the algorithm against noisy datasets with different percentages of additive noise variance

Noise Variance	Uniform Noise	Gaussian Noise
1%	88.6%	85.7%
2.5%	83.3%	82.0%
5%	77.0%	78.9%
10%	64.3%	73.1%

tributions, which were added to the synthetic medial surface. As can be seen, the percentage of misclassified deformations is acceptable up to 5% of additive noise.

4.6.2 LV's with multiple abnormalities

Although this method can classify the normal and abnormal subjects accurately but it considers only one abnormality patch on the left ventricle. Indeed, the two proposed measures, ANV and MP, yield good results, provided there is only one patch. Fig. 4.11 shows a patient having two abnormality on two different parts of the left ventricle. The experimental results show that the method wrongly classifies the subject as normal.

Fig. 4.12 illustrates a medial surface with two abnormalities, one on the apex and the other on the lateral wall. If we use the method as before, MP might locate inside the medial surface depending on the location of the patches. Furthermore, ANV might point to different directions at different time points. As a result, the LV's with two abnormalities will be classified as

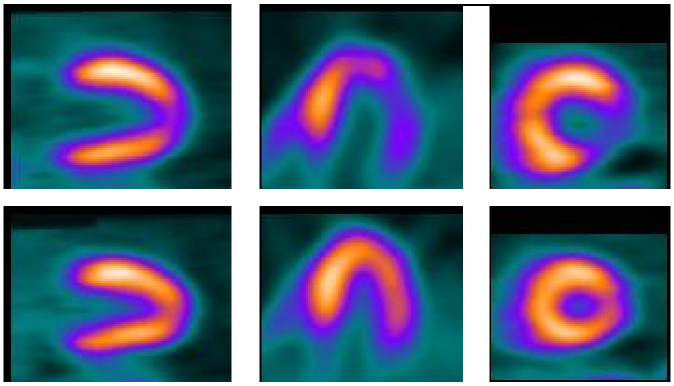

Figure 4.11: The gated images of a patient with apical ischemia and with abnormality on the lateral wall.

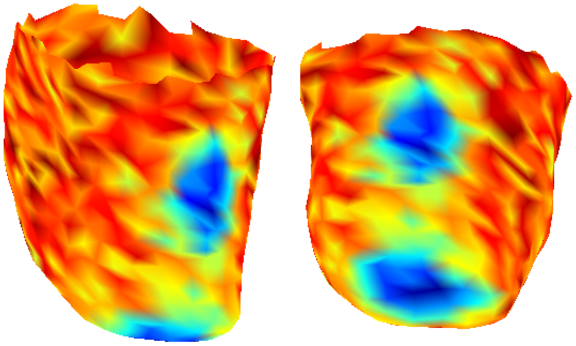

Figure 4.12: The medial surface of a subject having two abnormalities on the apex and the lateral wall shown as two blue patches. Different colors illustrate the thickness of the LV wall.

normal.

To tackle this problem, first we decompose the medial surface into some connected components based on the wall thickness. Then, the deformation path of each connected component is calculated as before. Therefore, a deformation path is constructed for each patch rather than for each subject. In this way, we convert the medial surface with two patches to two medial surfaces, each having one patch.

4.6.3 Abnormality size

Different patients might have abnormality patches of different sizes. Although, we did not aim to determine the size of the abnormality but measuring the size of the abnormality can reveal the severity of the disease. Fig. 4.13 shows a subject with small apical defect. Since the abnormality is small, so is its corresponding patch on the medial surface. We tested our method to see if it can differentiate very small or very large patches.

Fig. 4.14 shows the LV with three different patch sizes. If the patch is very large, MP of the

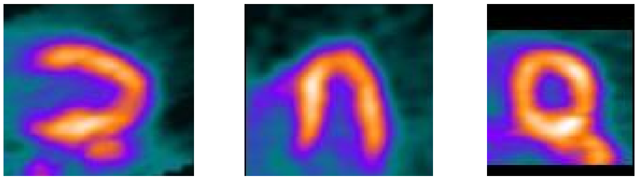

Figure 4.13: The gated images of a patient with a small apical defect.

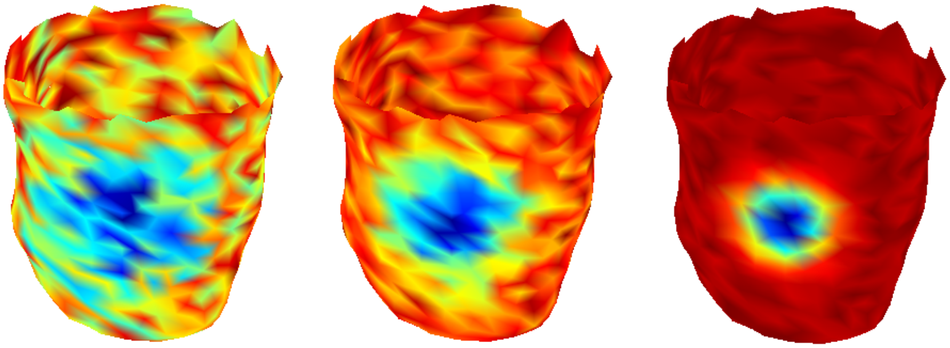

Figure 4.14: The medial surface classification is affected by the abnormality size. If the abnormality is large (Left), MP of the patch is inside the surface; on contrary, if it is small (Right), ANV might diverge away from each other.

patch might be inside the medial surface. If the patch is very small, ANV of the patch might not converge to the same direction, but the corresponding MP's are close to each other.

4.7 The Experimental Results of the Medial Surface Shape Space

As mentioned, the change of the thickness of the left ventricle wall over time is a useful feature to differentiate normal subjects from abnormal ones. Besides, automatic localization of the abnormality on the left ventricle is of great importance in the diagnosis procedure. To achieve these goals, the medial surface shape space is applied on the extracted left ventricle meshes as explained before.

There are some many researches for 3D medial surface extraction. At the first step, the medial surfaces of different poses are extracted and registered using the method proposed in [89]. Then the location of each pose in the medial surface shape space is calculated as mentioned.

Fig. 4.15.a shows the gated slice of a normal subject and Fig. 4.15.b illustrates the gated slice of a patient with anterior wall ischemia. As expected, the abnormality looks like a patch, thus the direction of ANV in the abnormality patch will not change so much over time, yet in the normal subject ANV's point to totally different directions.

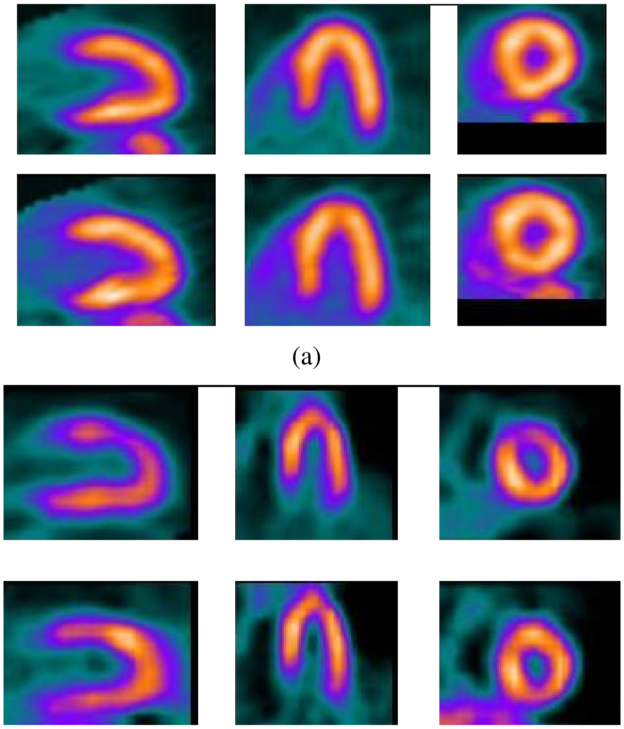

(a)

(b)

Figure 4.15: a) The gated images of a normal subject at two different time points, b) the gated images of a patient with anterior wall ischemia.

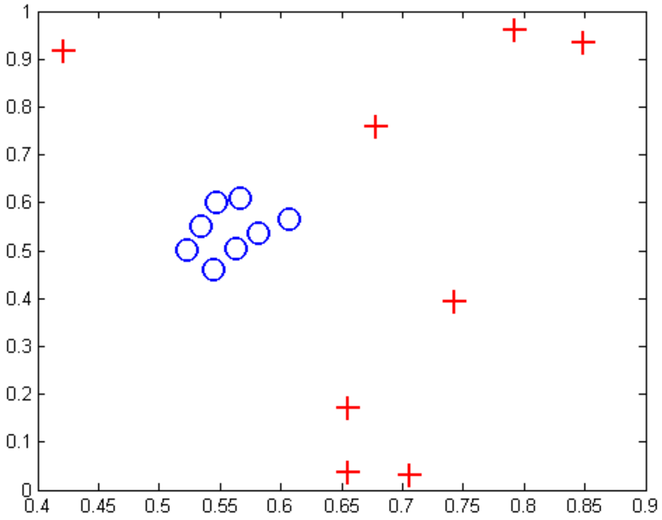

Figure 4.16: The projection of two normal (red crosses) and abnormal (blue circles) subjects onto the 2D plane using MDS. As seen, the normal deformation does not follow a specific deformation pattern and its points are far from each other compared with the abnormal subject.

The points corresponding to different poses of the LV medial surfaces might be close to each other, if there is an abnormality patch on the LV; otherwise, they are far from each other without following a specific deformation path on the 2D plane (Fig. 4.16). Indeed, the poses of the abnormal subject have roughly the same ANV and MP.

4.8 Summary

The medial surface shape space is presented to classify and compare deformations based on the changes of the wall thickness. Indeed, it is of great use to diagnose the left ventricles with cardiomyopathy in which a portion of the left ventricle wall does not work normally and the wall thickness is affected accordingly.

We employ the proportion of the thickness of the wall (*PT* values) which can spot the candidate locations with the abnormality. To confirm the performance of the *PT* values, two shape descriptors are introduced: 1. Average of the Normal Vectors (ANV), 2. Mean of the Positions (MP).

The shape space constructed based on these two shape descriptors makes use of the log map to determine the location of each pose in shape space and measure the distance between each pair of poses.

CHAPTER 5

CONCLUSION

5.1 Summary

The shape abstraction is of great importance to extract the information from the data. The shape space shows a remarkable potential towards this goal. Many researchers measure the dissimilarity between shapes after projection of the shapes onto the shape space and determine their distance using a metric which preserves the interested geometrical property. However, producing such a metric would be a great challenge.

In contrast, in this study, the concept of shape space is employed to classify different deformations. Given two different deforming objects, we try to determine the similarity between their deformations not the objects themselves.

In the first method, a metric based on the Riemannian metric definition is introduced, which preserves the curvature changes at each point of the manifold during the deformation, and a new quasi-conformal shape space is constructed based on the proposed metric. As the shape deforms, the corresponding points in shape space constitute a deformation path in a high dimensional space. As a result, to compare the deformations, one only needs to compare two high dimensional curves in a non-linear manifold. To make the deformation paths comparable in this non-linear space, we transfer them to the same part of the shape space manifold using the parallel transport method. Finally, the high dimensional curves are projected onto 2D or 3D space which makes it easier for the user to compare different deformations. The results on the synthetic datasets show that the quasi-conformal metric along with the proposed classification framework can classify and interpolate different non-conformal deformations.

Besides, the framework was employed to classify the deformation of the left ventricles. The experimental results show that this method can classify the normal and abnormal deformations, which makes it a valuable assistant tool for the heart diagnosis.

Although, the first method can classify the left ventricle deformation but it cannot spot the abnormality on the left ventricle. To address this drawback, we proposed the second method based the changes of the left ventricle wall. Basically, the thickness of the left ventricle wall is measured over time and proportion of the changes, called *PT* values, is compared at different parts of the left ventricle. To confirm the performance of the *PT* values, two shape descriptors are introduced: 1. Average of the Normal Vectors, 2. Mean of the Positions.

Finally the medial surface shape space is constructed which makes use of the log map. The results on the synthetic and the left ventricle datasets show that the medial surface shape space is a powerful method to classify different deformations and spot the abnormality on the left ventricle.

5.2 Future Work

1. **Diffusion Wavelet**: The *Diffusion Wavelets* arise from a multiresolution structure induced by a diffusion group acting on some space such as a manifold ([80][47]). Indeed, the wall thickness can be considered as a function on the medial axis manifold. The diffusion wavelet decomposition yields some bases representing the wall thickness function with different space and frequency properties. Since our goal is to classify the deformation of the LV and spot the abnormality on the LV, the Diffusion Wavelets decomposition shows good potential to construct the intended shape space. However, without common bases it is impossible to compare different medial surfaces and the challenge is to find some common wavelet bases to compare different deformations. Besides, different bases localize the abnormality depending on the size and location of the abnormality. However, selection of the best bases to spot the abnormality is another major challenge.

2. **Teichmüller shape space and Conformal Geometry**: Two surfaces are conformally equivalent if there exists an angle-preserving map between them. The Teichmüller space

for surfaces with the same topology is a finite-dimensional manifold, where each point represents a conformal equivalence class. Wang et.al. [101] used the shape index based on the Teichmüller space coordinates to produce the conformally equivalent classes, which is used to study brain morphometry.

As mentioned in the chapter 3, the quasi-conformal metric can measure the geodesic distance between normal and abnormal subjects. One potential approach is to use the shape index and generate the deformation path of each subject in the Teichmüller space for the deformation classification. However, there is one major drawback.

Since the extracted left ventricle mesh is a genus zero mesh with no boundary, the Teichmüller space cannot be constructed for it, unless we removed one patch of the mesh and make one boundary on the surface, which incurs some geometrical information loss. Furthermore, the choice of the correct patch which preserves the consistency among different subjects is another major challenge.

APPENDIX

Publications

- ***Journals***

  [1] **Vahid Taimouri**, Xin Liu, Zhaoqiang Lai, Chang Liu, Darshan Pai, and Jing Hua, "Colon Segmentation for Prepless Virtual Colonoscopy," IEEE Transactions on Information Technology in Biomedicine (TITB), Vol. 15, 2011.

  [2] **Vahid Taimouri**, and Jing Hua, "Deformations Analysis of in the Quasi-Conformal Shape Space," Submitted to IEEE Transactions on Visualization and Computer Graphics (TVCG).

  [3] **Vahid Taimouri**, and Jing Hua, "Deformation Classification in the Medial Surface Shape Space," Submitted to IEEE Transactions on Medical Imaging (TMI).

- ***Conferences***

  [4] **Vahid Taimouri**, Huiguang He, and Jing Hua, "Comparative Analysis of Quasi-Conformal Deformations in Shape Space," In Proceedings of the 13th International Conference on Medical Image Computing and Computer Assisted Intervention (MICCAI), 2010.

  [5] Zhaoqiang Lai, Jiaxi Hu, Chang Liu, **Vahid Taimouri**, Darshan Pai, Jiong Zhu, Jianrong Xu, and Jing Hua, "Intra-patient Supine-Prone Colon Registration in CT Colonography Using Shape Spectrum," In Proceedings of the 13th International Conference on Medical Image Computing and Computer Assisted Intervention (MICCAI), 2010 (Oral; Acceptance Rate: 5%).

  [6] **Vahid Taimouri**, and Jing Hua, "The Left Ventricle Classification Using the Shape Space of the Medial Surface," In preparation for submission to the International Conference on Medical Image Computing and Computer Assisted Intervention (MICCAI).

BIBLIOGRAPHY

[1] Restrictive cardiomyopathy. *Dorland's Medical Dictionary*.

[2] Ankerst, M., Kastenmller, G., Kriegel, H., and Seidl, T. Nearest neighbor classification in 3d protein databases. In *The 7th International Conference on Intelligent Systems for Molecular Biology (ISMB)* (1999), pp. 34–43.

[3] Azhari, H., Sideman, S., Weiss, J., Shapiro, E., Weisfeldt, M., Graves, W., Rogers, W., and Beyar, R. Three-dimensional mapping of acute ischemic regions using mri: Wall thickening versus motion analysis. *Amer. J. Physiol. 259* (1990), H1492–1503.

[4] Basri, R., Costa, L., Geiger, D., and Jacobs, D. Determining the similarity of deformable shapes. *Vision Research 38* (1998), 2365–2385.

[5] Bhattacharya, A. Nonparametric inference on shape spaces. *In JSM Proceedings* (2008).

[6] Bhattacharya, A. Perspectives in mathematical sciences, probability and statistics. *The Indian Journal of Statistics 70-A* (2008), 223–266.

[7] Bhattacharya, A., and Bhattacharya, R. Nonparametric statistics on manifolds with applications to shape spaces. *Pushing the Limits of Contemporary Statistics: Contributions in honor of J.K. Ghosh. IMS Collections 3* (2008), 282–301.

[8] Bhattacharya, A., and Bhattacharya, R. Statistics on manifolds with applications to shape spaces. *Perspectives in Mathematical Sciences, Probability and Statistics 3* (2008), 41–70.

[9] Bhattacharya, R., and Patrangenaru, V. Large sample theory of intrinsic and extrinsic sample means on manifolds. *Ann. Statist. 33* (2005), 1225–1259.

[10] BHATTACHARYAAND, A. Nonparametric statistics on manifolds with applications to shape spaces. *PhD Thesis* (2008).

[11] BIASOTTI, S., MARINI, S., MORTARA, M., PATANE, G., SPAGNUOLO, M., AND FALCIDIENO, B. 3d shape matching through topological structures. *In DGCI* (2003), 194–203.

[12] BIEDERMAN, I. Recognition-by-components: a theory of human image understanding. *Psychological Review 94* (1987), 115–147.

[13] BOLSON, E., AND SHEEHAN, F. Centersurface model for 3d analysis of regional left biventricular function. In *The IEEE Conference of Computers in Cardiology* (1993), pp. 735–738.

[14] BOOKSTEIN, F. Landmark methods for forms without landmarks: localizing group differences in outline shape. *Medical Image Analysis 1* (1997), 225–244.

[15] CHEN, D., TIAN, X., SHEN, Y., AND OUHYOUNG, M. On visual similarity based 3d model retrieval. *Computer Graphics Forum (EG 2003 Proceedings) 22* (2003).

[16] CHOW, B., AND LUO, F. Combinatorial ricci flows on surfaces. *J. Differential Geometry 63* (2003), 97–129.

[17] CICIRELLO, V., AND REGLI, W. Machining feature-based comparisons of mechanical parts. In *The IEEE International Conference on Shape Modeling and Applications* (2001), pp. 176–185.

[18] CLARYSSE, P., FRIBOULET, D., AND MAGNIN, I. Tracking geometrical descriptors on 3-d deformable surfaces: Application to the left-ventricular surface of the heart. *IEEE Trans. Med. Imag. 16* (1997), 392–404.

[19] Collins, C., and Stephenson, K. A circle packing algorithm. *Computational Geometry: Theory and Applications 25* (2003), 233–256.

[20] Corney, J., Rea, H., Clark, D., Pritchard, J., Breaks, M., and Macleod, R. Coarse filters for shape matching. *IEEE Computer Graphics and Applications 22* (2002), 65–74.

[21] Damon, J. On the smoothness and geometry of boundaries associated to skeletal structures i: Sufficient conditions for smoothness. *Annales de lInstitut Fourier 53* (2003), 1941–1985.

[22] Dryden, I., and Mardia, K. *Statistical Shape Analysis*. John Wiley and Sons, 1998.

[23] Duan, Y., Hua, J., and Qin, H. Interactive shape modeling using lagrangian surface flow. *The Visual Computer 21* (2005), 279–288.

[24] Duncan, J., Owen, R., Staib, L., and Anandan, P. Measurement of non-rigid motion using contour shape descriptors. *Computer Vision and Pattern Recognition 1*, 2 (1991), 318–324.

[25] Faber, T., Akers, M., Peshock, R., and Corbett, J. Three-dimensional motion and perfusion quantification in gated single-photon emission computed tomograms. *J. Nucl. Med. 32* (1991), 2311–2317.

[26] Frangi, A., Niessen, W., and Viergever, M. Three-dimensional modeling for functional analysis of cardiac images: A review. *IEEE Trans on Medical Imaging 20* (2001), 2–5.

[27] Friboulet, D., Magnin, I., Mathieu, C., Pommert, A., and Hoehne, K. Assessment and visualization of the curvature of the left ventricle from 3d medical images. *Comput. Med. Imag. 17* (1993), 257–262.

[28] Funck, W., Theisel, H., and Seidel, H. Vector field based shape deformations. *ACM Trans. on Graphics 25* (2006), 1118–1125.

[29] Funkhouser, T., Min, P., Kazhdan, M., Chen, J., Halderman, A., Dobkin, D., and Jacobs, D. A search engine for 3d models. *ACM Transactions on Graphics 22* (2003), 83–105.

[30] Gagvani, H., and Silver, D. Parameter controlled volume thinning. *Graphical Models and Image Processing 61* (1999), 149–164.

[31] Germano, G., Erel, J., Kiat, H., Kavanagh, P., and Berman, D. Quantitative lvef and qualitative regional function from gated 201-t1 perfusion spect. *J. Nucl. Med. 38* (1997), 749–754.

[32] Grenander, U. *General Pattern Theory*. Oxford University Press, 1993.

[33] Gu, X., Jin, M., Kim, J., and Yau, S. Computational conformal geometry applied in engineering fields. *ICCM 1* (2007), 72–94.

[34] Gu, X., Wang, Y., and Yau, S. Computing conformal invariants: Period matrices. *Communications in Information and Systems 3* (2004), 153–170.

[35] Gu, X., and Yau, S. Surface classification using conformal structures. In *Conference on Computer Vision and Pattern Recognition (CVPR)* (2003), pp. 701–708.

[36] Haker, S., Angenent, S., Tannenbaum, A., Kikinis, R., Sapiro, G., and Halle, M. Conformal surface parameterization for texture mapping. *IEEE Trans. on Visualization and Computer Graphics 6* (2000), 181–189.

[37] Hamilton, R. Three manifolds with positive ricci curvature. *J. Differential Geometry 17* (1982), 255–306.

[38] Hendricks, H., and Landsman, Z. Mean location and sample mean location on manifolds: Asymptotics, tests, confidence regions. *J. Multivariate Anal. 67* (1998), 227–243.

[39] Hilaga, M., Shinagawa, Y., and Kohmura, T. Topology matching for fully automatic similarity estimation of 3d shapes. *In SIGGRAPH* (2001), 203–212.

[40] Huang, J., Shi, X., Liu, X., Zhou, K., Guo, B., and Bao, H. Geometrically based potential energy for simulating deformable objects. *Visual Computer 22* (2006), 740–748.

[41] Huang, J., Shi, X., Liu, X., Zhou, K., Wei, L., Teng, S., Bao, H., Guo, B., and Shum, H. Subspace gradient domain mesh deformation. In *ACM Transaction on Graphics (TOG)* (2006).

[42] Hurdal, M., Stephenson, K., Bowers, P., Sumners, D., and Rottenberg, D. Coordinate systems for conformal cerebellar flat maps. *NeuroImage 11* (2000), S467.

[43] Huttenlocher, D., Klanderman, G., and Rucklidge, W. Comparing images using the hausdorff distance. *IEEE Trans. on Pattern Analysis and Machine Intelligence 15* (1993), 850–863.

[44] Iben, H., OBrien, J., and Demaine, E. Refolding planar polygons. In *Symposium on Computational Geometry* (2006), pp. 71–79.

[45] Iyer, N., Jayanti, S., Lou, K., Kalyanaraman, Y., and Ramani, K. Three dimensional shape searching: state-of-the-art review and future trends. *Computer-Aided Design 37* (2005), 509–530.

[46] Jameson, J., Kasper, D., Harrison, T., Braunwald, E., Fauci, A., Hauser, S., and Longo, D. *Harrison's principles of internal medicine.* New York: McGraw-Hill Medical Publishing Division, 2005.

[47] J.C. Bremer, R.R. Coifman, M. M. A. S. Diffusion wavelet packets. *Appl. Comp. Harm. Anal. 15* (2005), 95–112.

[48] Jin, M., Kim, J., Luo, F., and Gu, X. Discrete surface ricci flow. *IEEE Trans. on Visualization and Computer Graphics 14* (2008), 1030–1043.

[49] Jin, M., Luo, F., Yau, S., and Gu, X. Computing geodesic spectra of surfaces. In *ACM symposium on Solid and physical modeling* (2007), pp. 387–393.

[50] Jin, M., Zeng, W., Luo, F., and Gu, X. Computing teichmller shape space. *IEEE Trans. on Visualization and Computer Graphics (TVCG) 15* (2009), 504–517.

[51] Joshi, S., Kaziska, D., Srivastava, A., and Mio, W. Riemannian structures on shape spaces: A framework for statistical inferences. *In Statistics and Analysis of Shapes. Birkhauser, Boston, Massachusetts* (2006), 313–333.

[52] Jost, J. *Riemannian Geometry and Geometric Analysis*. Universitext, Springer, 2002.

[53] Kazhdan, M., Chazelle, B., Dobkin, D., Funkhouser, T., and Rusinkiewicz, S. A reflective symmetry descriptor for 3d models. *Algorithmica 38* (2004), 201–225.

[54] Kazhdan, M., Funkhouser, T., and Rusinkiewicz, S. Rotation invariant spherical harmonic representation of 3d shape descriptors. In *Eurographics/ACM SIGGRAPH symposium on Geometry processing* (2003), pp. 156–164.

[55] Kendall, D. The diffusion of shape. *Adv. Appl. Probab 9* (1977), 428–430.

[56] Kendall, D. Shape manifolds, procrustean metrics, and complex projective spaces. *Bull. London Math. Soc. 16* (1984), 81–121.

[57] KENNEDY, J., BAXLEY, W., FIGLEY, M., DODGE, H., AND BLACKMON, J. Quantitative angiocardiography: I. the normal left ventricle in man. *Circulation 34* (1966), 272–278.

[58] KILIAN, M., MITRA, N., AND POTTMANN, H. Geometric modeling in shape space. *ACM SIGGRAPH 26* (2007), 64–72.

[59] KOLMOGOROV, A. *Mathematics Of The 19th Century: Mathematical Logic, Algebra, Number Theory, Probability Theory*. Birkhuser, 2001.

[60] KORTGEN, M., PARK, G., NOVOTNI, M., AND KLEIN, R. 3d shape matching with 3d shape contexts. In *European Seminar on Computer Graphics* (2003).

[61] KRIM, H., YEZZI, A., AND EDS, A. Statistics and analysis of shapes. *Birkhauser, Boston, Massachusetts* (2006).

[62] LIPMAN, Y., COHEN-OR, D., GAL, R., AND LEVIN, D. Volume and shape preservation via moving frame manipulation. In *ACM Transaction on Graphics (TOG)* (2007), pp. 5–es.

[63] LIPMAN, Y., LEVIN, D., AND COHEN, D. Green coordinates. In *ACM Transactions on Graphics (TOG)* (2008).

[64] LORENZ, C., WALKER, E., MORGAN, V., KLEIN, S., AND JR., T. G. Normal human right and left ventricular mass, systolic function, and gender differences by cine magnetic resonance imaging. *J. Cardiovasc.Magn. Res. 1* (1999), 7–21.

[65] MARDIA, K., AND PATRANGENARU, V. Directions and projective shapes. *Ann. Statist. 33* (2005), 1666–1699.

[66] MCINERNEY, T., AND TERZOPOULOS, D. Deformable models in medical image analysis: A survey. *Medical Image Analysis 1*, 2 (1996), 91–108.

[67] McVeigh, E. Mri of myocardial function: Motion tracking techniques. *Magn. Reson. Imag. 14* (1996), 137–150.

[68] Miller, M., and Younes, L. Group actions, homeomorphisms, and matching: A general framework. *International Journal of Computer Vision 41* (2001), 61–84.

[69] Mio, W., and Srivastava, A. Elastic-string models for representation and analysis of planar shapes. In *The IEEE Conference on Computer Vision and Pattern Recognition (CVPR)* (2004), pp. 10–15.

[70] Nelson, T., Downey, D., Pretorius, D., and Fenster, A. *Three-Dimensional Ultrasound*. Philadelphia, PA: Lippincott Williams and Wilkins, 1999.

[71] Novotni, M., and Klein, R. 3d zernike descriptors for content based shape retrieval. In *The 8th ACM Symposium on Solid Modeling and Applications* (2003).

[72] Ohbuchi, R., Minamitani, T., and Takei, T. Shape-similarity search of 3d models by using enhanced shape functions. In *In Theory and Practice of Computer Graphics* (2003), pp. 97–104.

[73] Ohnesorge, B., Flohr, T., Becker, C., Knez, A., Kopp, A., Fukuda, K., and Reiser, M. Cardiac imaging with rapid, retrospective ecg synchronized multilevel spiral ct. *Der Radiologe 40* (2000), 111–117.

[74] Osada, R., Funkhouser, T., Chazelle, B., and Dobkin, D. Shape distributions. *ACM Transactions on Graphics 21* (2002), 807–832.

[75] Ozturk, C., and McVeigh, E. Four-dimensional b-spline based motion analysis of tagged cardiac mr images. *Proc. SPIE 3660* (1999), 46–56.

[76] PIZER, S., SIDDIQI, K., SZEKELY, G., DAMON, J., AND ZUCKER, S. Multiscale medial loci and their properties. *International Journal of Computer Vision 55* (2003), 155–179.

[77] REUTER, M., WOLTER, F., AND PEINECKE, N. Laplace-beltrami spectra as shape-dna of surfaces and solids. *Computer-Aided Design 38* (2006), 342–366.

[78] RICHARDSON, P., MCKENNA, W., AND BRISTOW, M. Report of the 1995 world health organization/international society and federation of cardiology task force on the definition and classification of cardiomyopathies harrison's principles of internal medicine. *Circulation 93* (1996), 841842.

[79] ROHLF, F. Shape statistics: Procrustes superimpositions and tangent spaces. *J. Classif. 16* (1999), 197–223.

[80] R.R. COIFMAN, M. M. Diffusion wavelets. *Appl. Comp. Harm. Anal. 21* (2006), 53–94.

[81] SACKS, M., CHUONG, C., TEMPLETON, G., AND PESHOCK, R. In vivo 3-d reconstruction and geometric characterization of the right ventricular free wall. *Ann. Biomed. Eng. 21* (1993), 263–275.

[82] SCLAROFF, S., AND PENTLAND, A. Modal matching for correspondence and recognition. *IEEE Trans on Pattern Analysis and Machine Intelligence 17* (1995), 545–561.

[83] SHARON, E., AND MUMFORD, D. 2d shape analysis using conformal mapping. In *The Conference on Computer Vision and Pattern Recognition (CVPR)* (2004), pp. 350–357.

[84] SHEEHAN, F., BOLSON, E., DODGE, H., MATHEY, D., SCHOFER, J., AND WOO, H. Advantages and applications of the centerline method for characterizing regional ventricular function. *Circulation 74* (1986), 293–305.

[85] SHUM, H., HEBERT, M., AND IKEUCHI, K. On 3d shape similarity. In *The Conference on Computer Vision and Pattern Recognition (CVPR)* (1996), pp. 526–531.

[86] SJOGREN, P. *Riemannska Symmetriska Rum.* Matematiska Institutionen, Chalmers Tekniska Hogskola och Goteborgs Universitet, 1987.

[87] SLICE, D. Landmark coordinates aligned by procrustes analysis do not lie in kendalls shape space. *Systematic Biology 50* (2001), 141–149.

[88] SUN, H., AVANTS, B., FRANGI, A., ORDAS, S., GEE, J., AND YUSHKEVICH, P. Branching medial models for cardiac shape representation. In *The IEEE International Symposium on Biomedical Imaging* (2008), pp. 1485–1488.

[89] SUN, H., AVANTS, B., FRANGI, A., SUKNO, F., GEE, J., AND YUSHKEVICH, P. Cardiac medial modeling and time-course heart wall thickness analysis. In *Medical Image Computing and Computer-Assisted Intervention (MICCAI)* (2008), pp. 766–773.

[90] SUNDAR, H., SILVER, D., GAGVANI, N., AND DICKENSON, S. Skeleton based shape matching and retrieval. In *the Shape Modeling International* (2003), pp. 130–139.

[91] TANGELDER, J., AND VELTKAMP, R. Polyhedral model retrieval using weighted point sets. *International Journal of Image and Graphics 3* (2003), 209–229.

[92] TANGELDER, J., AND VELTKAMP, R. A survey of content based 3d shape retrieval methods. *Multimedia Tools and Applications 39* (2008).

[93] TERRIBERRY, T., AND GERIG, A. A continuous 3-d medial shape model with branching. In *MICCAI Workshop Fndns. Comput. Anatomy (MFCA)* (2006).

[94] TERZOPOULOS, D., AND METAXAS, D. Dynamic 3d models with local and global deformations: deformable superquadrics. *IEEE Transaction on Pattern Analysis and Machine Intelligence 13* (1991), 703714.

[95] THALL, A. *Deformable Solid Modeling via Medial Sampling and Displacement Subdivision*. Ph.D. thesis, University of North Carolina at Chapel Hill, 2003.

[96] VLEUGELS, J., AND VELTKAMP, R. Efficient image retrieval through vantage objects. *Pattern Recognition 35* (2002), 69–80.

[97] VUILLE, C., AND WEYMAN, A. *Left ventricle I: General considerations, assessment of chamber size and function*. Principles and Practice of Echocardiography 2nd ed, A. E. Weyman, Ed. Philadelphia, PA: Lea and Febiger, 1994.

[98] WANG, S., JIN, M., GU, X., WANG, Y., AND SAMARAS, D. Conformal geometry and its applications on 3d shape matching recognition and stitching. *IEEE Transaction on Pattern Recognition and Machine Intelligenc* (2007).

[99] WUHRER, S., BOSE, P., SHU, C., OROURKE, J., AND BRUNTON, A. Morphing of triangular meshes in shape space. *International Journal of Shape Modeling (IJSM) 16* (2010), 195–212.

[100] XU, D., ZHANG, H., WANG, Q., AND BAO, H. Poisson shape interpolation. *Graphical Models 68* (2006), 268–281.

[101] Y. WANG, W DAI, Y. C. Y. G. T. C. A. T. P. T. Studying brain morphometry using conformal equivalence class. In *The IEEE International Conference on Computer Vision (ICCV)* (2009), pp. 2365–2372.

[102] YEZZI, A., AND MENNUCCI, A. Conformal metrics and true gradient flows for curves. In *Conference on Computer Vision* (2005), pp. 913–919.

[103] YUSHKEVICH, P., ZHANG, H., AND GEE, J. Continuous medial representation for anatomical structures. *IEEE Trans. Med. Imaging 25* (2006), 1547–1564.

[104] Zhang, C., and Chen, T. Efficient feature extraction for 2d/3d objects in mesh representation. *ICIP 3* (2001), 935–938.

[105] Zhou, K., Huang, J., Snyder, J., Liu, X., Bao, H., Guo, B., and Shum, H. Large mesh deformation using the volumetric graph laplacian. *ACM SIGGRAPH 24* (2005), 496–503.

[106] Zou, G., Hua, J., and Muzik, O. Non-rigid surface registration using spherical thinplate splines. *MICCAI 4791* (2007), 367–374.

ABSTRACT

SHAPE ANALYSIS IN SHAPE SPACE

by

VAHID TAIMOURI

May 2012

Advisor: Dr. Jing Hua

Major: Computer Science

Degree: Doctor of Philosophy

This study aims to classify different deformations based on the shape space concept. A shape space is a quotient space in which each point corresponds to a class of shapes. The shapes of each class are transformed to each other by a transformation group preserving a geometrical property in which we are interested. Therefore, each deformation is a curve on the high dimensional shape space manifold, and one can classify the deformations by comparison of their corresponding deformation curves in shape space. Towards this end, two classification methods are proposed.

In the first method, a quasi conformal shape space is constructed based on a novel quasi-conformal metric, which preserves the curvature changes at each vertex during the deformation. Besides, a classification framework is introduced for deformation classification. The results on synthetic and real datasets show the effectiveness of the metric to estimate the intrinsic geometry of the shape space manifold, and its ability to classify and interpolate different deformations.

In the second method, we introduce the medial surface shape space which classifies the deformations based on the medial surface and thickness of the shape. This shape space is based on the log map and uses two novel measures, *average of the normal vectors* and *mean of the positions*, to determine the distance between each pair of shapes on shape space.

We applied these methods to classify the left ventricle deformations. The experimental results shows that the first method can remarkably classify the normal and abnormal subjects but this method cannot spot the location of the abnormality. In contrast, the second method can discriminate healthy subjects from patients with cardiomyopathy, and also can spot the abnormality on the left ventricle, which makes it a valuable assistant tool for diagnostic purposes.

AUTOBIOGRAPHICAL STATEMENT

VAHID TAIMOURI

Vahid Taimouri is a Ph.D. candidate in Computer Science at Wayne State University, where he is also a research assistant in the Graphics and Imaging Laboratory. He received his B.Sc. and M.Sc. degrees in Biomedical Engineering, from Tehran Poly-Technique University and University of Tehran, Tehran, Iran, respectively. His research interests include computer graphics, image, visualization, and their applications to computer vision and medical imaging.